Bioactive Materials 35 (2024) 274–290

Contents lists available at ScienceDirect

Bioactive Materials

journal homepage: www.keaipublishing.com/en/journals/bioactive-materials

An Injectable silk-based hydrogel as a novel biomineralization seedbed for critical-sized bone defect regeneration

Yuhui Zhu[a,b,c,d,e,f,g,1], Hao Gu[a,b,c,d,e,f,g,1], Jiawei Yang[a,b,c,d,e,f,g], Anshuo Li[a,b,c,d,e,f,g], Lingli Hou[h], Mingliang Zhou[a,b,c,d,e,f,g,*], Xinquan Jiang[a,b,c,d,e,f,g,**]

[a] Department of Prosthodontics, Shanghai Ninth People's Hospital, Shanghai Jiao Tong University School of Medicine, No. 639 Zhizaoju Road, Shanghai, 200011, China
[b] College of Stomatology, Shanghai Jiao Tong University, No. 115 Jinzun Road, Shanghai, 200125, China
[c] National Center for Stomatology, No. 639 Zhizaoju Road, Shanghai, 200011, China
[d] National Clinical Research Center for Oral Diseases, No. 639 Zhizaoju Road, Shanghai, 200011, China
[e] Shanghai Key Laboratory of Stomatology, No. 639 Zhizaoju Road, Shanghai, 200011, China
[f] Shanghai Research Institute of Stomatology, No. 639 Zhizaoju Road, Shanghai, 200011, China
[g] Shanghai Engineering Research Center of Advanced Dental Technology and Materials, No. 115 Jinzun Road, Shanghai 200125, China
[h] Shanghai Institute of Precision Medicine, Shanghai Ninth People's Hospital, Shanghai Jiao Tong University School of Medicine, No. 115 Jinzun Road, Shanghai, 200125, China

ARTICLE INFO

Keywords:
Silk fibroin
Bone regeneration
Hydrogel
Biomineralization
Platelet-rich plasma

ABSTRACT

The healing process of critical-sized bone defects urges for a suitable biomineralization environment. However, the unsatisfying repair outcome usually results from a disturbed intricate milieu and the lack of in situ mineralization resources. In this work, we have developed a composite hydrogel that mimics the natural bone healing processes and serves as a seedbed for bone regeneration. The oxidized silk fibroin and fibrin are incorporated as rigid geogrids, and amorphous calcium phosphate (ACP) and platelet-rich plasma serve as the fertilizers and loam, respectively. Encouragingly, the seedbed hydrogel demonstrates excellent mechanical and biomineralization properties as a stable scaffold and promotes vascularized bone regeneration in vivo. Additionally, the seedbed serves a succinate-like function via the PI3K-Akt signaling pathway and subsequently orchestrates the mitochondrial calcium uptake, further converting the exogenous ACP into endogenous ACP. Additionally, the seedbed hydrogel realizes the succession of calcium resources and promotes the evolution of the biotemplate from fibrin to collagen. Therefore, our work has established a novel silk-based hydrogel that functions as an in-situ biomineralization seedbed, providing a new insight for critical-sized bone defect regeneration.

1. Introduction

Critical-sized bone defects, following trauma, congenital conditions and/or surgical procedures, exhibit an inability to heal spontaneously due to the lack of sufficient nutrient supply and high-quality blood clot [1,2]. These defects require intricate clinical intervention, including bone autograft or allograft transplantation, metallic bone fixation or bioactive growth factor application [1]. However, these approaches carry potential concerns for complications, the need for secondary surgeries, and the dosage considerations [3]. Thus, critical-sized bone defects entail substantial economic and considerable suffering on patients and remains a challenge in current clinical scenario. Tissue engineering, with a significant focus on biomimetic scaffolds that mimic natural biomineralization process, has emerged as a promising strategy to overcome these challenges [3–5]. Biomineralization is an effective approach extensively utilized for bone regeneration, especially in

Peer review under responsibility of KeAi Communications Co., Ltd.
* Corresponding author. Department of Prosthodontics, Shanghai Ninth People's Hospital, Shanghai Jiao Tong University School of Medicine, No. 639 Zhizaoju Road, Shanghai, 200011, China.
** Corresponding author. Department of Prosthodontics, Shanghai Ninth People's Hospital, Shanghai Jiao Tong University School of Medicine, No. 639 Zhizaoju Road, Shanghai, 200011, China.
E-mail addresses: mingliangzhou@aliyun.com (M. Zhou), xinquanjiang@aliyun.com (X. Jiang).
[1] These authors contributed equally.

https://doi.org/10.1016/j.bioactmat.2024.01.024
Received 10 November 2023; Received in revised form 10 January 2024; Accepted 25 January 2024

repairing critical-sized bone defects [6,7]. However, the primary components of biomineralization, such as collagen, face numerous challenges including rapid degradation and weak mechanical strength [6,8], which may need to align better with the pace of bone regeneration. Thus, novel and innovative biomineralization strategies await development to conquer this issue.

Inspired by natural tissue regeneration, a finely tuned biomineralization system should involve a dynamic fibrin-collagen template transition in a well-orchestrated manner [9]. In the initial stage of physiological bone repair, the hematoma not only provides a stable fibrin template, but also acts as a reservoir of multiple growth factors for cell migration, as well as a platform for cell adhesion [10]. A mature hematoma can lead to a satisfying bone mineralization and healing outcome [11]. However, establishing a stable and high-quality blood clot is particularly difficult in critical-sized defects due to the lack of blood supply [2]. Drawing inspiration from the intricate process of natural bone healing, an engineered biomineralization seedbed should be supported by a robust scaffold, effectively serving as geogrids. The scaffold is complemented by an organic fibrin network, akin to nutrient-rich loam, and supplied with biomineralization nutrients, acting as fertilizers, to encourage optimal bone growth and regeneration.

Building upon the concept of an ideal biomineralization seedbed, silk fibroin (SF) emerges as a promising support biomaterial due to its outstanding mechanical properties and biocompatibility [12]. SF exhibits mechanical strength surpassing numerous natural templates, such as cellulose, chitosan and collagen [13–15]. The favorable degradation rate and continuous support of SF effectively compensate for the inherent looseness of fibrin clots in large bone defects [16,17]. A recent study has underscored the efficacy of SF as a mineralization scaffold [18], attributed to its distinctive hydrophilic amorphous acidic spacers [19]. The oxidized SF (OxSF), which introduces additional carboxyl groups, enhances the electronegativity and theoretically provides more favorable sites for mineralization [14,20]. Notably, OxSF can also act as the negative-charged stabilizer to guarantee the presence of sufficient amorphous calcium phosphate (ACP) [14,21]. Hence, we propose that OxSF is an excellent candidate for creating a biomineralization template and rigid geogrids within the seedbed to facilitate bone regeneration.

Apart from the geogrids, the rapid biomineralization requires abundant organic and inorganic components, much like the role of the loam and fertilizers in a seedbed. Platelet-rich plasma (PRP) is recognized as an ideal endogenous seedbed due to its natural assembly of fibrin and abundant growth factors [22,23]. The integration of OxSF's strength and PRP's resilience potentially paves the way for a double network structure, mutually enhance their mechanical properties [22,24,25]. Concurrently, the growth factors embedded in the PRP function as organic nutrients in the seedbed to promote cell migration and angiogenesis for subsequent intrinsic bone regeneration [23,26]. Besides, ACP is a precursor of bone minerals and serves as the main inorganic component for biomineralization [27]. However, its instability remains a challenging obstacle to create an integrated system in critical-sized bone defects. To address this issue, we not only utilized OxSF as a mineralization template scaffold, but also innovatively employed OxSF as an ACP stabilizer, leveraging its aspartic acid in the side chain [14], and thereby creating an integrated seedbed system with inorganic and organic nutrients, specifically ACP and PRP. These components intricately collaborated and induced biomineralization synergistically. Therefore, our designated seedbed hydrogel incorporates a mineralizable scaffold template, with a high-concentration enrichment of inorganic ACP and organic growth factors, providing a fertile ground for excellent regeneration in critical-sized bone defects.

In this work, we have developed a novel silk-based double-network hydrogel that serves as a biomineralization seedbed, integrating the essential organic and inorganic elements for natural bone healing. The seedbed hydrogel proved to be highly effective in stabilizing the ACP and exhibited inherent mineralization capability both in vitro and in vivo. It significantly enhanced osteogenesis and angiogenesis in vitro and effectively promoted successful vascularized bone regeneration in vivo. We gained invaluable insights into the collaboration between the scaffold and the embedded clues through RNA sequencing (RNAseq). This analysis revealed the intricate mechanism behind the intracellular transportation of succinate and its orchestration with mitochondrial calcium uptake, effectively converting the exogenous ACP into endogenous ACP (Scheme 1). Taken together, we have designed a delicate double-network hydrogel that functions as an in-situ seedbed, completes with mineralization templates and biomineralization components. This pioneering approach holds great promise for enhancing critical-sized bone defect regeneration.

2. Materials and methods

2.1. Animals and cell culture

Sprague-Dawely (SD) rats were provided by the Ninth People's Hospital Animal Center (Shanghai, China). All the experiment procedures were approved by the Animal Care and Experiment Committee of the Ninth People's Hospital and animals were treated under standard specific pathogen-free laboratory conditions. The animal license number is SH9H-2019-A169-1.

Rat bone marrow stromal cells (BMSCs) were isolated from 4-week-old SD rats as previously described. Briefly, cells were washed from femurs and tibias and cultured in high-glucose Dulbecco's modified Eagle Medium (DMEM; Hyclone, USA) with 10 % fetal bovine serum (Gibco, USA) at 37 °C in a 5 % CO_2 atmosphere. Cells at passage 2–5 were used for the subsequent experiments. Human umbilical vein endothelial cells (HUVECs) were purchased from Cyagen Biosciences (Guangzhou, China) and cultured in endothelial cell medium (ECM; HUVEC-90011, Cyagen, China) at 37 °C in a 5 % CO_2 atmosphere.

For establishing the calvarial defect model, 36 SD rats were intraperitoneally anesthetized 50 mg/kg Zoletil50 (Virbac, France) and 12.5 mg/kg Dexdomitor (Orion, Finland). The dorsal cranium was exposed and a full thickness bone defect with a diameter of 5 mm was made at the center of each parietal bone. Composite hydrogels were injected to the defect sites. Samples were harvested 8 weeks and 12 weeks after surgery for osteogenesis evaluation. The samples for histological transmission electron microscopy (TEM) analysis were harvested at day 14. For degradation test in vivo, critical-sized cranial defects (diameter = 5 mm) were created in 12 C57BL/6 mice and samples were harvested at day 7 for histological analysis.

2.2. Preparation of composite hydrogels

SF was prepared following the protocol described by Rockwood et al. [12]. Briefly, *Bombyx mori* cocoon was degummed by boiling in 0.02 M Na_2CO_3 solution for 30 min and dried in an oven at 60 °C overnight. The degummed silk was dissolved in 9.3 M LiBr solution at 60 °C and dialyzed to remove the salts for 3 days. The silk fibroin was stored and utilized after lyophilization. The oxidized silk fibroin (OxSF) was obtained by adding NaClO solution (2 mmol/g of SF) under an alkaline environment (pH = 10) with continuously addition of 0.5 M NaOH solution [20]. The reaction was terminated by adjusting the pH to 7 when no consumption of NaOH was further necessary. The solution was further dialyzed for 2 days and stored after lyophilization. The oxidized silk fibroin with amorphous calcium phosphate (OxSF/ACP) was prepared via a mixture of 5 wt% OxSF and 5 wt% poly-aspartic acid sodium salt solution (pAsp; P303238, Aladdin, China). $CaCl_2$ and Na_2HPO_4 were added in a powder form with vigorous stirring. PRP was prepared from the whole blood of SD rats (weighed 250–300 g) by cardiac puncture after deep anesthesia with Zoletil50 and Dexdomitor, as mentioned above. 5 mL whole blood was collected in the anticoagulation tube (Kangjian, China). The blood samples were centrifugated at 900 rpm for 5 min and the top layer was transferred into a sterile tube and

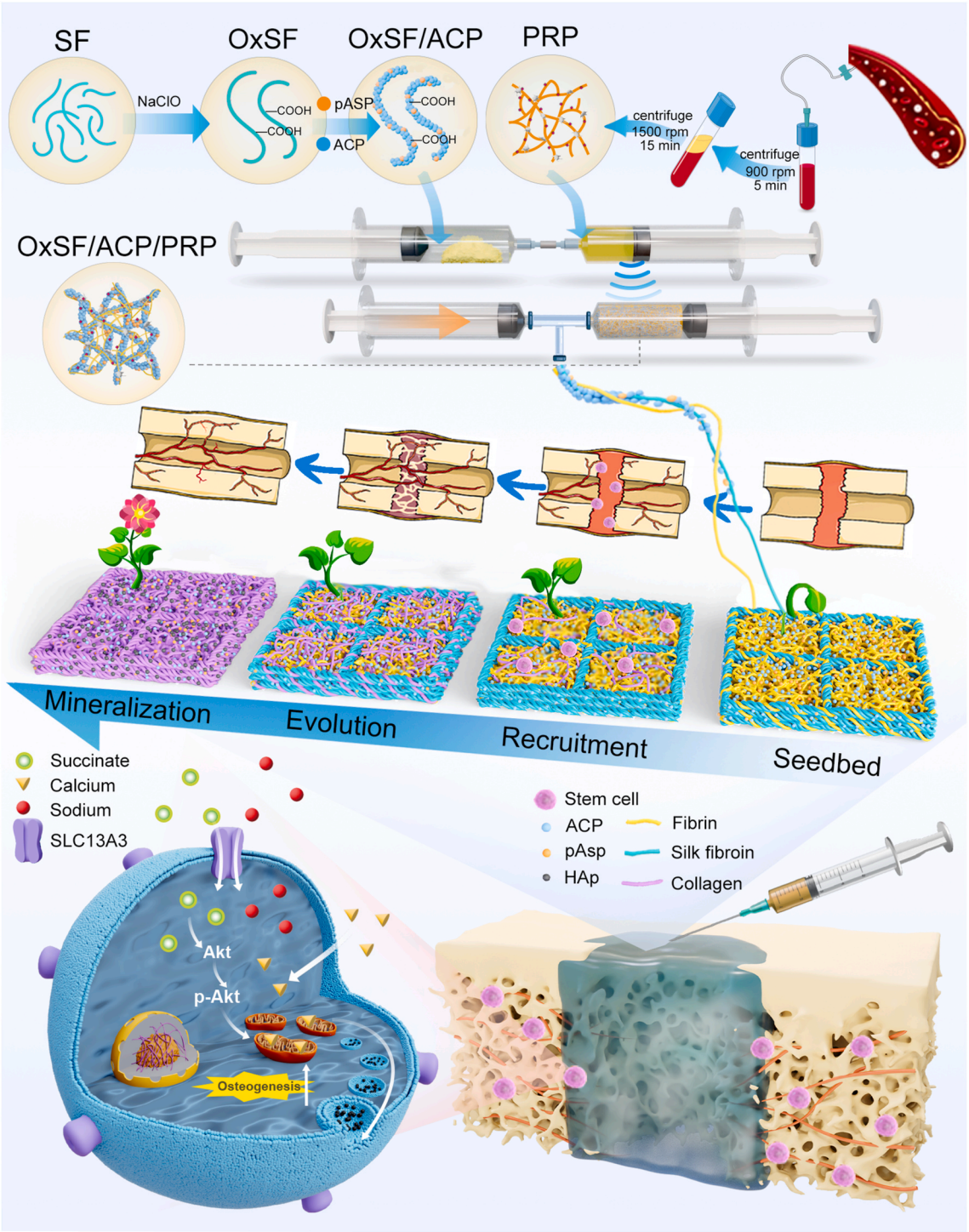

Scheme 1. Schematic diagram showing the preparation of the seedbed hydrogel and the procedure and mechanism of the seedbed hydrogel in vascularized bone regeneration. SF, silk fibroin; OxSF, oxidized silk fibroin; pAsp, polyaspartic acid; ACP, amorphous calcium phosphate; PRP, platelet-rich plasma; HAp, hydroxyapatite.

centrifuged at 1500 rpm for 15 min. The PRP was collected in the liquid form and mixed with lyophilized OxSF/ACP powder to construct the evenly-distributed liquid OxSF/ACP/PRP composite hydrogel by repetitive extrusion thoroughly. Sonication was used to trigger the solidification and polymerization of the SF and OxSF network. 1 mL hydrogel solution was sonicated at 50 % amplitude for 15 s using an ultrasonic processor (VCX130, SONICS & MATERIALS, USA).

2.3. Mineral precipitations

For in vitro mineralization of composite hydrogels, a mineralization solution was prepared as described by de Wildt et al. [19]. Briefly, a 10 × simulated body fluid (SBF) solution was prepared following the protocol of Tas and Bhaduri [26] and 100 μg/mL pAsp solution and a final concentration of 10 mM $NaHCO_3$ was added into the solution. The hydrogels were solidified as cylinders (10 mm in diameter, 8 mm in height) and incubated in 40 mL mineralization solution for 2 weeks on a

shaker at 50 rpm with a solution replenishment after 1 week. After mineralization, the hydrogel scaffolds were washed in ultrapure water for 3 × 15 min and preserved in ultrapure water for further analysis.

2.4. Injectability assessment

The liquid hydrogel was transferred into the glass vials immediately after sonication and incubated in 37 °C. The gelation process was observed at 5 min and 30 min after the sonication by tilting the vials. The injectability of the gelated hydrogel was assessed by extrusion from the 1 mL syringe.

2.5. Fourier-transform infrared spectroscopy (FTIR)

The structural functional groups were characterized by FTIR (Thermo Scientific Nicolet iS5, USA) in the IR range between 400 and 4000 cm^{-1}. The analysis was performed with the attenuated total reflectance (ATR) method.

2.6. Calculation of degree of substitution (DS)

The degree of substitution was measured and calculated by the content of amino acid in SF and OxSF. The amino acids were hydrolyzed from the SF and OxSF solution according to GB 5009.124–2016. The amino acids were examined using the amino acid analyzer (sykam S433D, Germany). The amount of the protein was evaluated by the Kjeldahl method. DS was calculated according to the following formula:

$$DS\ (\%) = \frac{Amount\ of\ the\ substituted\ Serine}{Total\ amount\ of\ Serine} \times 100\ \%$$

2.7. Morphological characterization

The microstructure morphology of unmineralized and mineralized hydrogels were observed using scanning electron microscopy (SEM, Sigma 300, Zeiss, Germany). To observe the morphology, the hydrogels were fixed with 2.5 % glutaraldehyde, dehydrated using gradient ethanol, sprayed with platinum and observed with SEM under an acceleration voltage at 3 kV. The pore size was analyzed by ImageJ as described by Wolosyzk et al. [2]. The energy-dispersive X-ray (EDX) analysis was performed under 2 kV for element analysis. The internal microstructures of the hydrogels were observed by TEM (Talos L120C, Thermo Scientific, USA). The hydrogels were dehydrated using the same protocol as SEM and embedded in epoxy resin for sectioning and staining. The samples were observed and selected area electron diffraction (SAED) was performed at 120 kV.

2.8. Rheological and mechanical tests

The rheological tests of hydrogels were measured at 37 °C using a rotational rheometer (ThermoFisher HAAKE, USA) with a parallel plate of 35 mm diameter and an operating gap distance of 0.5 mm. Time sweep tests were performed using a constant strain of 1 %. Viscosity measurements were performed at a constant strain of 1 %. Recovery properties were characterized by three cycles of repetitive stress at either 5 % strain or at 1 % strain, each lasting for 60s. The compressive strength was measured by a universal testing machine (HY-0230, Shanghai Hengyi, China). Different composite hydrogels were prepared into cylinders (10 mm in diameter, 8 mm in height) and tested with a strain rate of 2 mm/min. The stress at a strain of 50 % was measured for quantification.

2.9. Release of inorganic and organic components

The samples of SF, OxSF, OxSF/ACP and OxSF/ACP/PRP were immersed in 6 mL ultrapure water at 37 °C with a shaking speed of 50 rpm. The supernatant was collected after 1, 4, 7 and 14 days, respectively. The calcium concentrations were measured by the Calcium Colorimetric Assay Kit (Beyotime, China). To measure the amount of growth factors released from PRP and OxSF/ACP/PRP, the samples were immersed in 2 mL ultrapure water with a shaking speed of 50 rpm for 1, 4, 7 and 14 days, respectively. The concentrations of PDGF-BB and VEGF in the supernatant were tested using the commercial enzyme-linked immunosorbent assay (ELISA) kits (J&L Biological, China) according to the manufacturer's instructions. The pH value of the supernatant was measured by an acidimeter (S470-USP/EP). Succinate concentration was evaluated on a column of cation-exchange resin in a high-speed liquid chromatography (HPLC, LC-20AD, Shimadzu, Japan).

2.10. Degradation test in vitro

The hydrogels were immersed in PBS supplemented with 1 μg/mL type I collagenase at 37 °C [28]. The hydrogels were taken out and weighed at day 4, 7 and 14, respectively. The enzyme solution was replaced with a freshly prepared solution.

2.11. X-ray diffractometry (XRD)

An X-ray diffractometer (Rigaku D/mak-2200PC, Japan) was utilized to present the crystal structures of inorganics in different hydrogels. The unmineralized and mineralized hydrogels were lyophilized and powdered for XRD analysis. The Cu target was carried out between 5° and 90° with a scan speed of 5° per minute. Mineral composition was identified referencing the International Diffraction Data Center Spectrum Database.

2.12. Zeta potential measurement

Zeta potentials of SF and OxSF were evaluated in the MES solution using a DLS method-based zeta-meter (Malvern Zetasizer Nano ZS90, UK). The measurement was conducted at the room temperature.

2.13. Microcomputed tomography (μCT)

For in vitro scaffold mineralization, the scaffold samples were scanned wet as described by de Wildt et al. [19]. The scanner (μCT50, Scanco Medical, Switzerland) was set at 45 kVp, 200 μA, an integration time of 300 ms and an isotropic resolution of 11.4 μm.

For in vivo bone defect regeneration assessment, the cranial samples were dissected and fixed for 24 h with 4 % paraformaldehyde (PFA) in 4 °C and kept in 75 % ethanol for high-resolution μCT scanning. The scanner was set at 70 kVp, 200 μA, an integration time of 400 ms and a resolution of 10.0 μm.

2.14. Cell viability and proliferation

For the biocompatibility tests, BMSCs and HUVECs were either seeded in a 96-well plate and cultured with different conditioned medium, or seeded on different composite hydrogels directly. The conditioned medium was prepared by immersing 1 mL sonicated hydrogel in 10 mL DMEM with 10 % FBS at 37 °C for 24 h. The cell viability was assessed by the calcein-AM and propidium iodide double staining (Beyotime, China) 24 h after seeding. The proliferation rate was determined by cell counting kit-8 (CCK8, Yeasen, China) at day 1 and 4.

2.15. Alkaline phosphatase (ALP) staining and activity

BMSCs were seeded in a 24-well plate and cultured with the conditioned medium for 7 days for ALP staining and activity assay. The ALP staining was performed using the BCIP/NBT Alkaline Phosphatase Color Development Kit (Beyotime, China). The ALP semiquantitative assay was performed using the ALP Assay Kit (Beyotime, China) following the

manufacturer's instructions. The absorbance values measured at 405 nm were converted to ALP activity using standard curve, and further calculated based on the total protein, which was measured by the Enhanced BCA Assay Kit (Beyotime, China).

2.16. Alizarin red S (ARS) staining

BMSCs were seeded in a 24-well plate and cultured with the conditioned medium for 21 days for ARS staining. The cells were fixed with 4 % PFA for 15 min and stained with ARS solution (Beyotime, China).

2.17. Quantitative reverse transcription-polymerase chain reaction (RT-qPCR)

BMSCs were cultured in a 6-well plate with the conditioned medium for 7 days. Total RNA was extracted with RNAiso Plus (Takara, Japan) and reverse-transcribed into complementary DNA with PrimeScript™ RT reagent Kit (Takara, Japan) for subsequent qPCR analysis. Subsequent quantitative gene analysis was performed using Hieff® qPCR SYBR Green Master Mix (Yeasen, China) by the Roche Molecular Light Cycler (Roche, Switzerland). Relative gene quantitation was assessed by the $2^{-\Delta\Delta CT}$ method. Primers are listed in Table S1.

2.18. Western blotting

To measure the protein expression, BMSCs cultured with different conditioned medium were collected and lysed using RIPA buffer (Beyotime, China) with 1 mM PMSF on ice. The supernatants were obtained after centrifugation at 12000×*g* for 15 min at 4 °C. The total protein concentration was measured by BCA kit (Beyotime, China). Total cell lysates were separated by 4 %–16 % Bis-Tris gels and blotted on polyvinylidene difluoride membranes (Millipore, USA). The PVDF membrane was incubated with primary antibodies against COL1A1 (1:1000 dilution, E8I9Z, Cell Signaling Technology, USA), OPN (1:1000 dilution, AKm2A1, Santa Cruz, USA), SLC13A3 (1:500 dilution, 26184-1-AP, Proteintech, China), MKX (1:500 dilution, sc-515878, Santa Cruz, USA), Akt and phospho-Akt (1:1000 dilution, 9272S, 9271T, Cell Signaling Technology, USA) and GAPDH (1:1000 dilution, D16H11, Cell Signaling Technology, USA), respectively, and further incubated with appropriate horseradish peroxidase-conjugated secondary antibodies. The protein expression was finally visualized by enhanced chemiluminescence (ECL Kit; Thermo Fisher, USA).

2.19. Immunofluorescence (IF) staining

A primary antibody targeting Runt-related transcription factor 2 (RUNX2) (1:8000 dilution, D1L7F, Cell Signaling Technology, USA) was used to evaluate the cellular osteogenic differentiation. The Alexa Fluor 594-conjugated donkey anti-rabbit secondary antibody (1:250 dilution, 34212ES60, Yeasen, China) was used to visualize the immunofluorescence staining and the cell skeleton and nuclei were further stained with FITC-phalloidin (Yeasen, China) and 4',6-diamidino-2-phenylindole, pihydrochloride (DAPI; Solarbio, China), respectively.

In vivo staining of OPN (1:200 dilution, AKm2A1, Santa Cruz, USA), CD31 (1:2000 dilution, ab182981, Abcam, USA) and DAPI (Solarbio, China) was performed using an IHC Fluorescence kit (Recordbio Biological Technology, Shanghai, China) based on the tyramide signal amplification (TSA) technology according to the manufacturer's instructions. The images were captured with a confocal laser scanning microscopy (Leica, Germany).

2.20. Cell migration

Wound healing assay and Transwell migration assay were performed to evaluate the influence of different composite hydrogels of chemotaxis on HUVECs. HUVECs were seeded on a 6-well plate and starved with low serum (1 %) medium 24 h before the wound healing test. A 1 mL pipette tip was used to create scratches and floating cells and debris were removed with PBS. Then, HUVECs were cultured with corresponding hydrogel conditioned medium. The cell migration into the wound was assessed by the inverted microscopy after 12 h. The healing ratio was calculated by the area covered by the migrating cells measured by Image J.

HUVECs were starved with low serum (1 %) medium overnight and seeded at a concentration of 1×10^5/mL in the upper chamber of the Transwell culture inserts (8 μm in pore size, Corning, USA). The lower chamber was filled with different composite hydrogel-conditioned medium. After 24 h incubation, the lower surface of the Transwell inserts were fixed with 4 % PFA for 10 min and stained with 0.1 % crystal violet for 15 min. The migratory cells were captured by an inverted microscopy and the number of migratory cells was counted using Image J.

2.21. Tube formation assay

HUVECs were seeded on a 96-well plate coated with 60 μL Matrigel (Corning, USA) per well at a concentration of 3×10^5/mL. The HUVECs were cultured in different conditioned medium at 37 °C in the 5 % CO_2 air incubator for 6 h. Tube structures were observed under the inverted microscopy (Ti–U, Nikon, Japan). Number of nodes, meshes and branches were quantified using Image J software to assess the tube formation.

2.22. Histological and histomorphometry analysis

Histological analysis was performed as previously described [27]. Briefly, the calvarial samples were fixed in 4 % paraformaldehyde in 4 °C for 24 h and decalcified in 20 % EDTA solution. The decalcified samples were dehydrated in gradient ethanol and embedded in paraffin for subsequent histological examinations. The hematoxylin-eosin (HE) staining and Masson Trichrome staining were conducted using commercial experiment kits (Solarbio, China) following the manufacturer's instruction.

The TEM samples were collected at day 14 and fixed with 2.5 % glutaraldehyde and 1 % osmium. The samples were subsequently dehydrated with gradient alcohol and embedded in epoxy resin for sectioning and staining. The samples were observed at 120 kV.

2.23. Transcriptome sequencing and data processing

For RNAseq, BMSCs were cultured in the 10 cm petri dishes (to a concentration of 1×10^7) with different hydrogel-conditioned medium. Total RNA was collected with RNAiso Plus. The RNAseq assay was performed by Shanghai Biotree Biotech. The libraries were sequenced on Illumina Novaseq™ 6000 and 150 bp paired-end reads were generated.

2.24. Detection of succinate uptake

The uptake of succinate was visualized by the addition of FITC-conjugated succinate (1 mM, Qiyue Biology, China) in the conditioned medium. The inhibition of SLC13A3 was induced by N-(P-amylcinnamoyl)anthranilic acid (NAA, TargetMol, USA) at the concentration of 100 μM. After 24 h cultivation, cells were fixed in 4 % PFA and stained with TRTIC Phalloidin (1:250 dilution, Yeasen, China) for cytoskeletion and DAPI for nuclei visualization. The images were captured with the confocal laser scanning microscopy.

2.25. Detection of calcium distribution

The detection of calcium distribution was visualized by staining with Fluo4-AM (37 °C for 30 min; Dojindo, Japan) and Rhod2-AM (4 °C for 30 min; Dojindo, Japan) for the intracellular and intramitochondrial calcium, respectively. The nuclei were visualized by staining with

Hoechst 33342 (Dojindo, Japan).

2.26. Statistical analysis

Data are represented as the mean ± standard deviation. Statistical analysis was performed by GraphPad Prism 9 software (GraphPad, USA). Statistically significant differences were indicated by $p < 0.05$ as determined by one-way analysis of variance (ANOVA) followed by Turkey's post-hoc test for multiple comparisons.

3. Results and discussion

3.1. Preparation and characterization of the seedbed hydrogel

The preparation of the seedbed hydrogel is visually displayed in Scheme 1. In brief, the geogrid of the seedbed was constructed using a carboxyl-group-enriched support network (OxSF), which served as the template for biomineralization. Subsequently, the polyelectrolyte and ACP (pAsp-ACP) were introduced as fertilizers into the seedbed (OxSF/ACP). Following this, concentrated PRP and an adequate amount of the upper liquid plasma were mixed with lyophilized components, acting as a loam, to generate an all-in-one seedbed hydrogel (OxSF/ACP/PRP) for subsequent biomineralization.

Although silk fibroin possesses self-assembly capability, the natural gelation process is uncontrollable and usually takes months, limiting its immediate clinical application [12]. Hence, we employed a simple sonication method to expedite the gelation process (Scheme 1). Additionally, calcium, added as the fertilizer, acts as the enhancer of β-sheet formation of the silk fibroin [29], and the essential coagulation factor in PRP formation [28]. To verify the acceleration effect, we monitored the gelation time of different hydrogels after sonication. All hydrogels exhibited a flowable state immediately after sonication, which corresponded to their shear thinning behaviors (Fig. S1). Notably, both the OxSF/ACP and OxSF/ACP/PRP groups displayed a reduced gelation time (~5 min), in contrast to the SF (~30 min) and the OxSF (~10 min) group (Fig. 1A). The improved gelation process provided a window of opportunity for shape adaptation, allowing the hydrogel to be injected and molded into irregular shapes that address diverse bone defects before reaching complete gelation (Fig. 1B and Fig. S2).

To evaluate the mechanical properties of the seedbed hydrogel, we conducted an oscillatory time sweep measurement on different hydrogels. Remarkably, the OxSF/ACP/PRP seedbed hydrogel exhibited a rapid increase in G′ value (storage modulus) after ~ 3 min and finally reached the plateau at G' ≈ 7.6 kPa. The fast sol-gel transition highlighted its exceptional strength and efficiency during gelation. In comparison, G' values of the OxSF/ACP and OxSF gradually reached ~3.6 kPa and ~1.7 kPa, respectively. Particularly, the SF started the gelation after ~18 min and the storage modulus of SF reached the plateau of ~2.5 kPa until 120 min after sonication (Fig. 1C and Fig. S3). This result aligned with our observation of the gelation process (Fig. 1A). The seedbed hydrogel was capable to recover under the repetitive stress, along with the highest elastic modulus compared to the other hydrogels (Fig. S4). Consistently, the OxSF/ACP/PRP group showed enhanced compressive stress compared to the other groups (Fig. 1C), which conformed to our initial double-network design [24]. Although OxSF exhibited lower mechanical strength than SF, which might be attributed to the lower molecular weight caused by oxidation procedure, the OxSF/ACP rescued the decrease in the stress. The enhanced mechanical strength of the seedbed hydrogel greatly exceeded that of the natural hematoma fibrin clot, which was regarded as the minimum strength during the bone healing process [2,9]. These results suggested that the seedbed hydrogel met the requirements in the complex mechanical environment of bone defect sites.

Subsequently, we utilized SEM to directly observe the morphological changes resulting from each step in the seedbed hydrogel development. As illustrated in Fig. 1D, the OxSF presented a rigid porous network compared to the SF, which might be attributed to the self-assembly micelles caused by the carboxylation of OxSF [14]. The addition of ACP introduced small inorganic nano-spheres into the seedbed hydrogel [30]. Furthermore, the incorporation of PRP not only facilitated the interconnection of the silk fibers and fibrin, but also introduced activated platelets into the biomineralization system (Fig. 1D). As the structure of PRP is delicate, all the samples for SEM were prepared through gradient alcohol and critical point drying dehydration. In such conditions we observed the mean pore size of hydrogels. The mean pore size of the seedbed hydrogel reached 181.17 ± 83.74 nm, while that of SF, OxSF and OxSF/ACP was 97.53 ± 28 0.13 nm, 65.15 ± 19.70 nm and 87.24 ± 43.19 nm, respectively (Fig. S5). The pore size of the seedbed hydrogel closely mimicked the natural hematoma fibrin clot, particularly in the context of normal healing [2]. The EDX mappings confirmed the presence of abundant calcium and phosphorus, the major elements associated with biomineralization, with both elements being evenly distributed (Fig. 1E).

To further explore the composite of the seedbed hydrogel, FTIR was conducted to examine the functional groups within the materials. The FTIR spectrum of OxSF showed typical absorption peaks at 1700 cm^{-1} and 1265 cm^{-1}, corresponding to the carboxyl vibration peaks [20]. The carboxylation of SF also resulted in the conformation change that was associated with increased β-sheets, which led to the shift of the peak from 1640 cm^{-1} to 1620 cm^{-1} [20]. Upon the introduction of ACP, a minor absorption peak emerged at ~600 cm^{-1} and a characteristic phosphate band (-PO_4^{3-}) appeared at ~1019 cm^{-1} (Fig. 1F). Additionally, we calculated the degree of substitution of carboxyl group in OxSF by examining the content of the amino acid. As DS was closely related to the concentration of NaClO used for oxidation and we followed the optimal NaClO concentration (2 mM/g SF), the DS for OxSF in our study was 61.07 ± 9.23 %. This DS would lead to the concentration of carboxyl group to 1.36 ± 0.07 mM/g SF, which aligned with the statistics reported by Zheng et al. [20].

The seedbed hydrogel possessed sufficient nutritional fertilizer, composed of inorganic and organic components. The hydrogel functioned as a calcium reservoir and maintained continuous calcium release for up to 14 days, reaching a cumulative concentration of 117.34 ± 6.33 μg/mL (Fig. 1G), which was found to be optimal for biomineralization [31]. Besides, the seedbed hydrogel neutralized the acidic environment caused by the carboxyl group within the OxSF network by elevating the pH value from 6.6 to 7.2 (Fig. S6). The addition of PRP introduced various bioactive growth factors. Hereby, we demonstrated the cumulative release of vascular endothelial growth factor (VEGF) and platelet-derived growth factor (PDGF). Compared to the loam PRP itself, the seedbed hydrogel helped increase the loading concentration of VEGF and PDGF, and turned a short-term robust release into a long-term sustained release profile (Fig. 1G). The modified release pattern can be attributed to the hydrogel's slow degradation and its dense double-network structure [22], formed by the synergic interpenetration of the geogrid and loam. This delicate design could effectively retain the nutrients inside while resisting external erosion, ensuring a controlled and extended nutrient release of the seedbed over time.

To explore the degradation profile of the hydrogels, an enzymatic degradation test was conducted in vitro. The degradation rate was preferably synchronized with the rate of mineral deposition [1]. As bone mineralization can be observed as early as 2 weeks in vivo [32], we conducted the degradation studies within 14 days. The remaining weight of the seedbed hydrogel reached 36.12 % of its original weight at day 4, 25.97 % at day 7 and 23.47 % at day 14, respectively (Fig. S7). This accelerated degradation characteristic could be attributed to the rapid degradation of PRP in the seedbed hydrogel, and the remaining porous structure led to a larger surface area [33]. The in vivo degradation in the cranial defect 7 days post-surgery appeared to align with the degradation rate observed in vitro (Fig. S8).

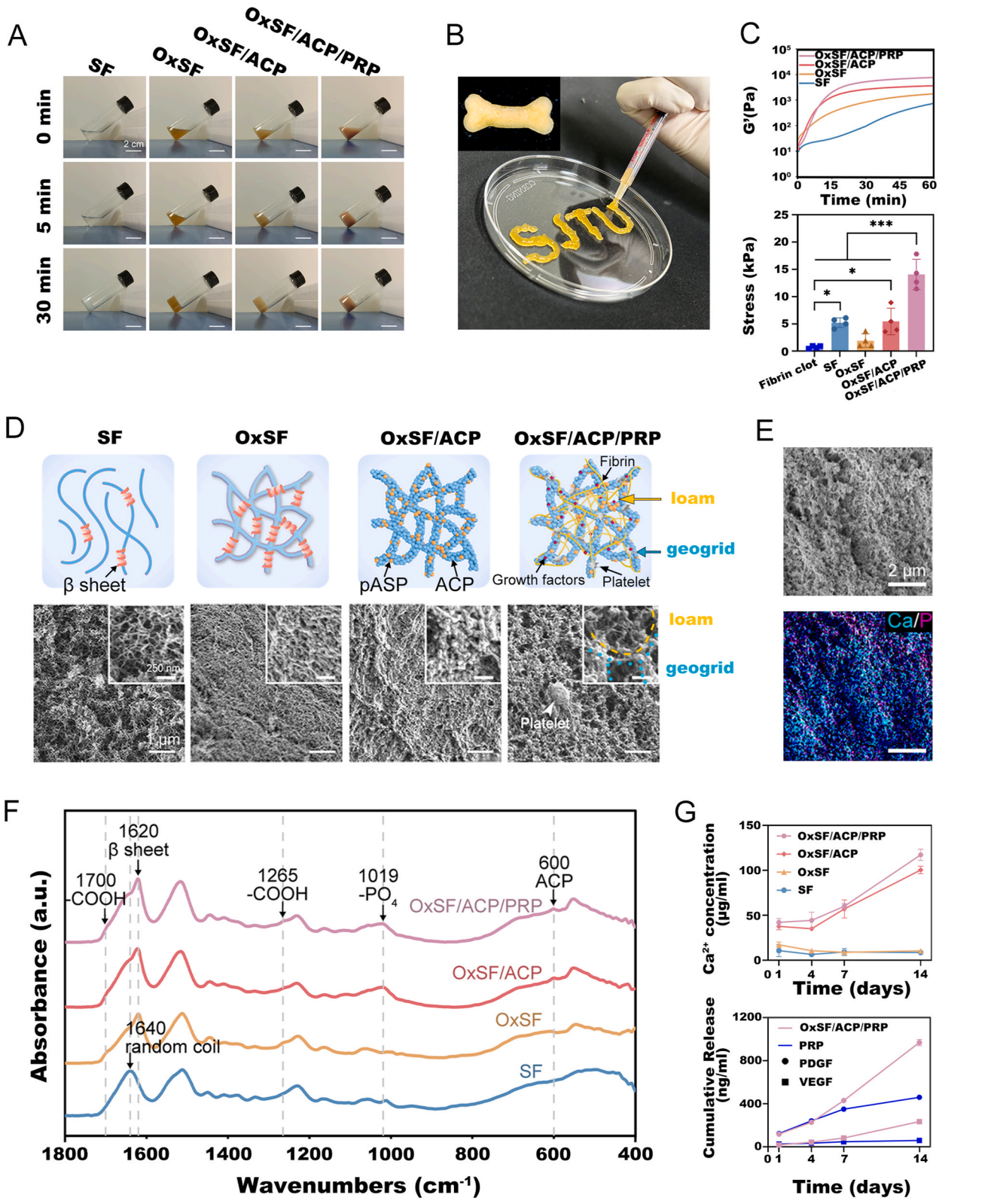

Fig. 1. Characterization of the biomineralization seedbed. A) Images showing the gelation process after sonication (Scale bar = 2 cm). B) Images reflecting the injectability and moldability of the OxSF/ACP/PRP seedbed hydrogel. C) Rheology of oscillatory time sweeps of different composite hydrogels (n = 4), and stress at a strain of 50 % of the hematoma fibrin clot and different composite hydrogels (n = 4). D) The schematic diagrams and SEM images of different composite hydrogels (Scale bar = 1 μm in main figures, and scale bar = 250 nm in insets). E) EDX analysis of the OxSF/ACP/PRP seedbed (Scale bar = 2 μm). F) FTIR spectra of different composite hydrogels. G) The calcium concentration in the supernatant of different composite hydrogels at day 1, 4, 7 and 14 (n = 3), and cumulative release of PDGF-BB and VEGF in the supernatant of the PRP and the OxSF/ACP/PRP seedbed hydrogel (n = 3). Error bars, mean ± standard deviation, *p < 0.05, ***p < 0.001.

3.2. In vitro biomineralization of the seedbed hydrogel

To further elucidate the biomineralization capacity of the composite hydrogels, we utilized 10 × simulated body fluid to create a biomineralization milieu in vitro for 14 days. We employed XRD to measure the crystallization in unmineralized and mineralized hydrogels and to characterize the status of calcium and phosphate in the composite hydrogels in situ. XRD analysis revealed that unmineralized hydrogels were all in an amorphous state. Specifically, the composite hydrogel seedbed displayed an amorphous diffraction peak of ACP at 2θ = 24.04° and a broad peak of SF at 2θ = 20.66°. The mineralized seedbed hydrogel exhibited sharp peaks at 2θ = 26.2° or 31.8°, indicative of crystalized hydroxyapatite [6], while the other groups displayed predominantly poorly crystalline apatite (Fig. 2A).

To evaluate the morphological changes before and after the mineralization, we conducted SEM and TEM analysis. SEM images demonstrated the fine and homogenous single fiber of the unmineralized composite hydrogels. After mineralization, the seedbed hydrogel exhibited a greater abundance and coarser morphology of mineralized fibers than the other groups (Fig. 2B). Consistently, TEM images revealed that the unmineralized OxSF/ACP and OxSF/ACP/PRP displayed dense, separate and uniform sized clusters in the fiber bundles. Interestingly, the seedbed hydrogel exhibited a thicker fiber bundle with a diameter of ~10 μm while the other groups reached merely 1–2 μm (Fig. 2C). This may be attributed to the intertwining and merging of SF fiber bundles and fibrins [34,35], along with the mineral stabilization and deposition promoted by plasma proteins in PRP [36]. The SAED analysis further identified the amorphous feature of OxSF/ACP/PRP, consistent with the XRD result (Fig. S9). After mineralization, the seedbed hydrogel exhibited the presence of well-defined crystallites, uniquely aligned along the fibers compared to the other groups (Fig. 2C). These results validated a transition from ACP to crystalized

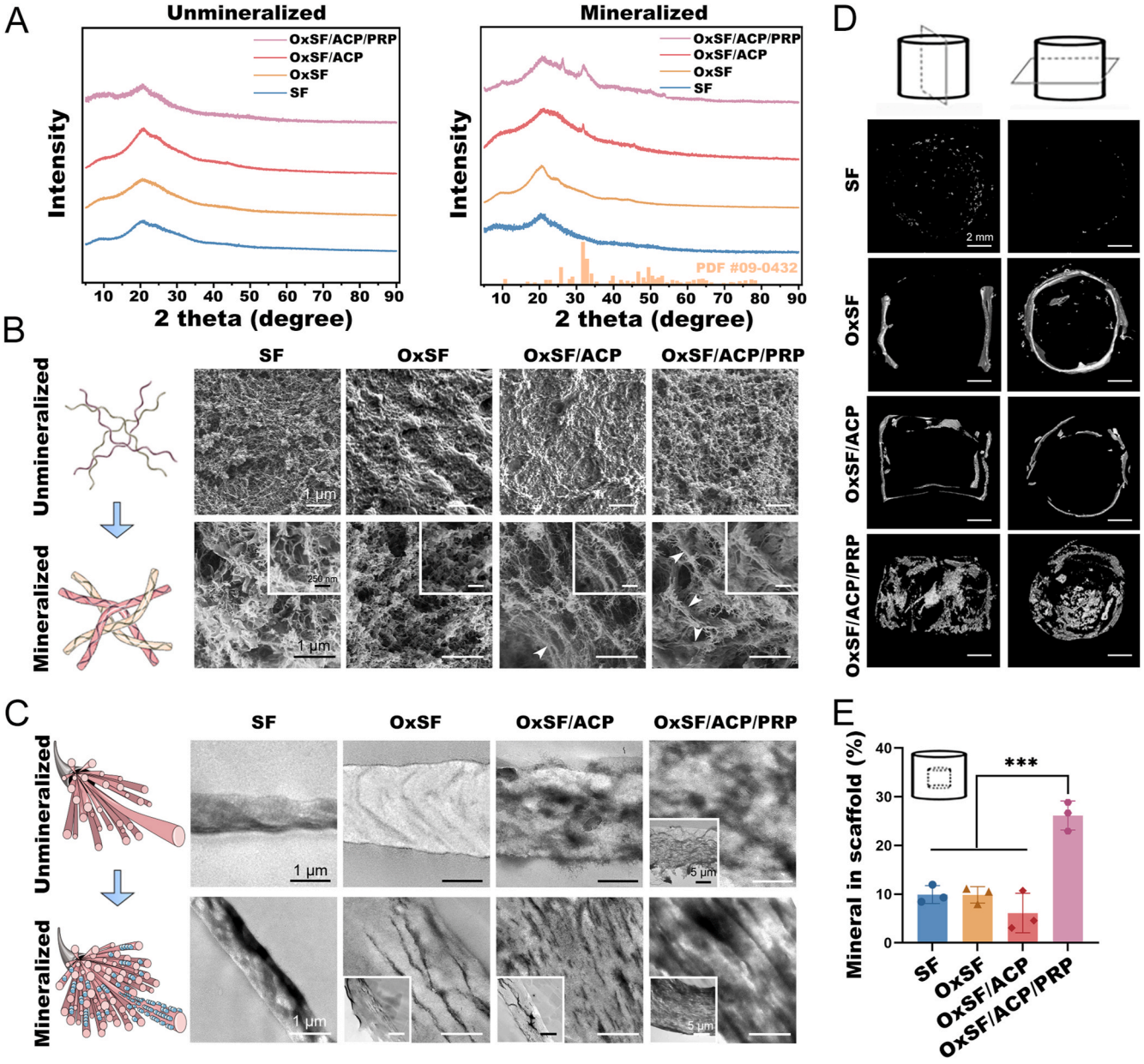

Fig. 2. In vitro biomineralization of the seedbed hydrogel. A) XRD patterns of unmineralized and mineralized composite hydrogels (orange columns represent XRD pattern of hydroxyapatite). B) SEM images of unmineralized and mineralized composite hydrogel and the schematic diagrams. C) TEM images of unmineralized and mineralized composite hydrogels and schematic diagrams. D) Reconstruction of μCT of mineralized composite hydrogels. E) Quantitative analysis of the mineral distribution (n = 3). Error bars, mean ± standard deviation, ***p < 0.001.

hydroxyapatite in the composite hydrogel seedbed in vitro.

The longitudinal and cross section of the mineralized materials assessed by μCT scanning demonstrated that the mineralized seedbed exhibited a more uniform distribution of mineralized particles, while in the mineralized SF, the particles were sporadically dispersed. Moreover, the particles tended to accumulate on the surface of the mineralized OxSF and OxSF/ACP (Fig. 2D). The longitudinal and cross-section views of the mineralized materials illustrated an evenly distributed mineralization pattern in the seedbed, which may be associated with the ability of plasma proteins in the loam to stabilize and concentrate the fertilizer ACP in vitro [36]. The quantification of the mineral precipitated at the center revealed an evenly distributed mineralization pattern in the seedbed (Fig. 2E), which solves the diffusion problem in the mineralization of the silk-based hydrogels [32]. The superior mineralization capability of the seedbed hydrogel was expected partly because of the significant reduction of the zeta potential of OxSF, from -17.13 ± 0.35 mV to -23.8 ± 1.41 mV (Fig. S10). Moreover, the optimal degradation pattern and porosity of the seedbed hydrogel could contribute to the mineral distribution, even if the OxSF/ACP/PRP group shared similar mineral content with the OxSF/ACP group (Fig. S5, S7 and S8), which showed lower mineral distribution than SF and OxSF with no statistical differences. This mineralization pattern induced by the seedbed hydrogel, closely mirrors the natural biomineralization evolution observed in bone healing.

3.3. Biocompatibility and osteogenesis of the seedbed hydrogel

The interaction between the implanted materials and cells, as well as their osteogenic capacity, are fundamental aspects of biomineralization. The seedbed hydrogel exhibited excellent biocompatibility with BMSCs (Fig. 3A and B, and Fig. S11). Notably, the cells cultured on the surface of the seedbed hydrogel displayed a stretched and extended morphology, in contrast to the contracted and spherical shape and aggregated cell clusters observed in the other groups (Fig. S11). These results suggested a tendency for cells to adhere and survive on the seedbed hydrogel, indicating the fabricated composite hydrogel has the potential to emulate the physiological microenvironment and facilitate subsequent cell differentiation [33]. However, regarding the interference of the inherent color and the imaging surface of the hydrogels, conditioned medium was employed to create a uniformed cultivation environment in vitro. Consistent with the live/dead staining result, the seedbed hydrogel showed a significant potential to improve the innate proliferating ability at day 1 and day 4 verified by the CCK8 assay (Fig. 3C). This could be attributed to an early proliferative effect of the organic fertilizers in PRP loam, which can be observed as soon as 24 h [37].

To examine the osteogenic properties of the composite hydrogels, we cultured the BMSCs with the hydrogel-conditioned medium and examined the expression of osteogenic markers at multiple levels. At the gene level, the mRNA expression of osteogenic markers, including *Alp*, *Osx* and *Col1a1*, significantly increased in the seedbed hydrogel (Fig. 3D). The ALP activity was significantly enhanced by the seedbed hydrogel at day 7 compared to the other groups (Fig. 3E), indicating considerable regulation of its osteogenic differentiation. Accordingly, the ALP staining showed that the seedbed hydrogel exhibited the most prominent capacity to induce the expression of ALP at day 7 (Fig. 3F and Fig. S12). ARS staining at day 21 also confirmed the superior calcium nodule formation in the seedbed hydrogel (Fig. 3G and Fig. S13). To further confirm its osteogenic properties at the protein level, we conducted immunofluorescent staining and Western Blot analysis. The expression of RUNX2, a marker for osteoblast differentiation, was significantly higher in BMSCs cultured with the seedbed hydrogel (Fig. 3H and I). Additionally, the seedbed hydrogel had increased level of COL1A1 and OPN protein (Fig. 3J). This suggested the collagen formation and the development of a biotemplate in the seedbed. These results confirmed that the OxSF/ACP/PRP seedbed hydrogel was effective in inducing osteogenic differentiation of BMSCs in vitro.

3.4. Angiogenesis of the seedbed hydrogel

In the repair of critical-sized bone defects, vascularization poses a significant challenge that may hinder favorable repair outcomes [38]. As the capillary vessels can facilitate the effective exchange of oxygen and nutrients, an ideal seedbed for bone regeneration must be highly vascularized [38]. The scratch wound healing assay displayed a significantly improved migratory ability of HUVECs induced by the seedbed hydrogel (Fig. 4A) and the healing ratio reached 77.24 % in 12 h. In contrast, the healing ratio induced by SF and OxSF merely reached 46.52 % and 61.22 %, respectively (Fig. 4B). Moreover, a Transwell system was applied to demonstrate the migration of HUVECs excluding the influence of cell proliferation. Corresponding to the scratch assay, the HUVECs co-cultured with the composite hydrogel seedbed system outnumbered other groups significantly (Fig. 4C and D). These results verified the potent ability of the seedbed system to promote endothelial cell migration.

To further investigate the direct angiogenic potential of the seedbed hydrogel, we conducted a tube formation on the surface of Matrigel with HUVECs. As expected, a remarkable increase in the endothelial tube was observed in the OxSF/ACP/PRP group (Fig. 4E). The number of nodes and branches significantly increased induced by the seedbed hydrogel (Fig. S14) and the number of meshes tripled from 14.3 to 44.3 compared to the SF group (Fig. 4F), indicating PRP and ACP are effective enhancers of angiogenesis. Additionally, the angiogenic genes were conjointly upregulated, including *Vegf*, *Ang1*, *Emcn* and *Pdgf* (Fig. 4G). Interestingly, ACP possessed a dual effect of osteogenesis and angiogenesis [39,40], which explained the increased tube formation and higher expression of angiogenic markers before the addition of PRP into the seedbed hydrogel. Both PRP and ACP could promote sprouting angiogenesis factor, *Vegf*, while PRP did not promote additional *Pdgf* expression, as this might potentially inhibit the process of vessel formation [41].

Therefore, the seedbed hydrogel, notably the integrated loam and fertilizers, contributes greatly to vascularization, which establishes a vital connection with the host by facilitating the exchange of nutrients and biological signals for subsequent bone regeneration.

3.5. In vivo osteogenic and angiogenic properties of the seedbed hydrogel

To explore the in vivo osteogenic and angiogenic capacities of the seedbed hydrogel, we created critical-sized cranial defects (diameter = 5 mm) in SD rats. The hydrogels were injected to the defect sites as demonstrated in Fig. S2. The samples were collected for analysis after the implantation of different composite hydrogels for 8 and 12 weeks. As expected, μCT analysis revealed that the seedbed hydrogel was capable of inducing substantial new bone formation from 8 weeks post-surgery. Meanwhile, the other groups merely led to scattered bone regeneration (Fig. 5A). Quantitative analysis revealed that the bone volume/tissue volume (BV/TV) in the seedbed hydrogel reached 55.18 ± 0.8 %. In contrast, the BV/TV values of the SF, OxSF and OxSF/ACP groups were 29.93 ± 1.1 %, 32.11 ± 1.38 % and 39.65 ± 6.27 %, respectively. (Fig. 5B). The bone mineral density (BMD) also significantly increased to 203.58 mgHA/cc in the seedbed hydrogel (Fig. 5B). At 12 weeks post-surgery, the BV/TV value of the seedbed group remained ~57 %, which suggested that the bone repair in the OxSF/ACP/OCP group had stabilized by 8 weeks. Meanwhile, the BV/TV increased to 39.9 % and 46.01 % in the OxSF and OxSF/ACP groups by 12 weeks, respectively. Additionally, the BMD of the seedbed hydrogel reached 420.32 mgHA/cc (Fig. 5C and D). These results indicated that the seedbed hydrogel significantly improved and accelerated the bone repair process, possibly due to its inherent mineralization, as well as early-stage vascularization [42].

To verify our hypothesis, we employed HE staining and Masson Trichrome to evaluate the microstructure of the new bone formation at

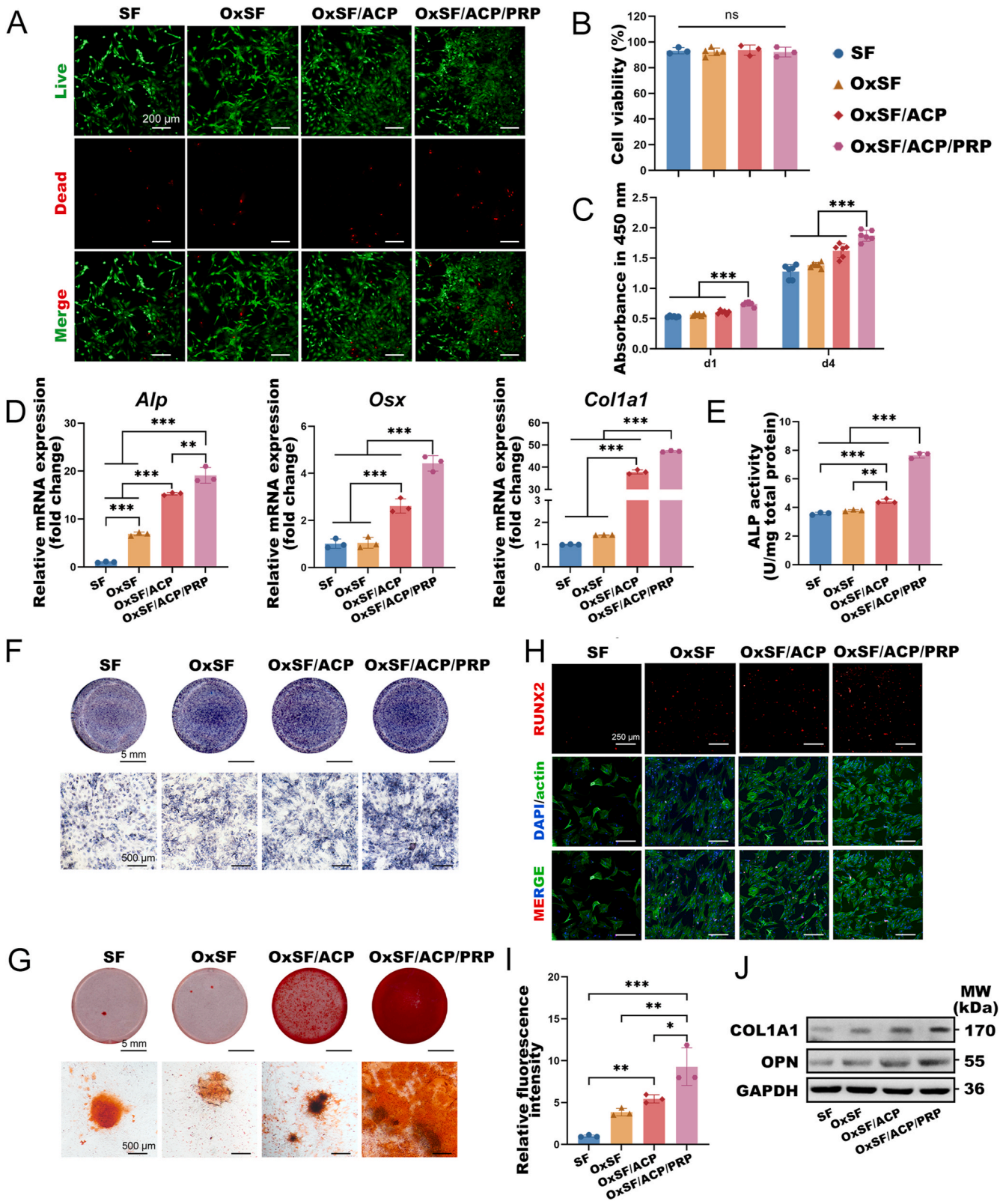

Fig. 3. Biocompatibility and osteogenic capability of the seedbed hydrogel in vitro. A) Live/dead staining of BMSCs cultured with conditioned medium of composite hydrogels and B) the quantitative analysis of cell viability (n = 3). C) Quantitative analysis of cell proliferation of BMSCs by CCK8 (n = 6). D) Relative mRNA expression of the osteogenic genes *Alp*, *Osx* and *Col1a1* in BMSCs (n = 3). E) ALP activity per mg total protein of BMSCs (n = 3). F) ALP staining of BMSCs at day 7 (Scale bar = 5 mm and 500 μm, respectively). G) ARS staining of BMSCs at day 21 (Scale bar = 5 mm and 500 μm, respectively). H) Immunofluorescent staining of RUNX2 of BMSCs and I) the relative fluorescence intensity (n = 3). J) Expression of osteogenic proteins OPN and COL1A1 of BMSCs (normalization using GAPDH). Error bars, mean ± standard deviation, *p < 0.05, **p < 0.01, ***p < 0.001.

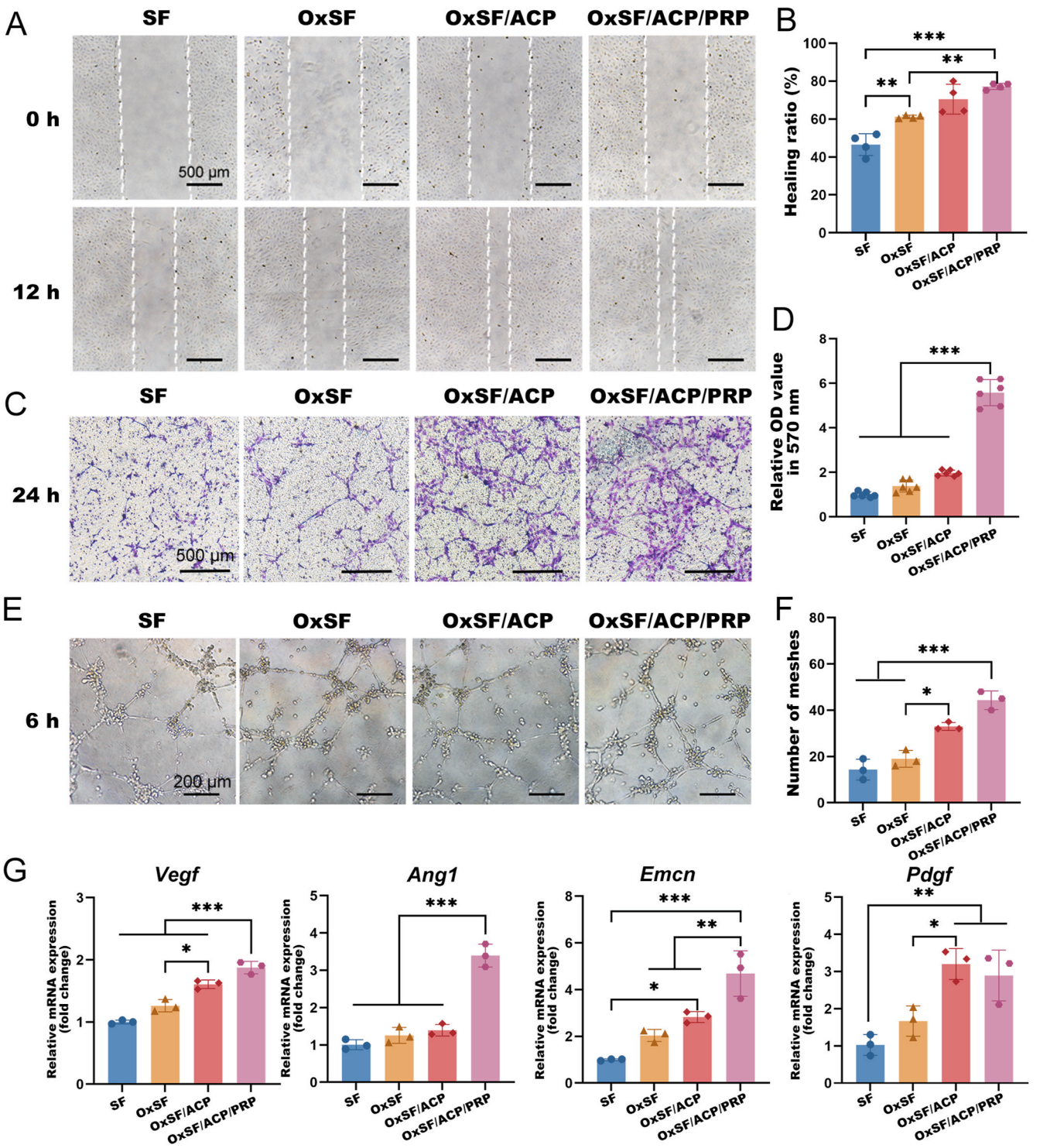

Fig. 4. Angiogenesis induced by the seedbed hydrogel in vitro. A) Scratch wound healing of HUVECs cultured with conditioned medium of the composite hydrogels at 12 h (Scale bar = 500 μm) and B) the healing ratio (n = 4). C) Vertical migration ability of HUVECs evaluated by the Transwell system (Scale bar = 500 μm) and D) quantitative analysis of the migrated cells (n = 6). E) Tube formation of HUVECs cultured on the Matrigel with conditioned medium (Scale bar = 200 μm) and F) the quantitative analysis by the number of meshes (n = 3). G) Relative mRNA expression of the angiogenic genes *Vegf*, *Ang1*, *Emcn* and *Pdgf* (n = 3). Error bars, mean ± standard deviation, *p < 0.05, **p < 0.01, ***p < 0.001.

the histological level. Results showed that the largest area of bone regeneration was found in the seedbed group. In contrast, the OxSF/ACP, OxSF and SF groups showed relatively small new bone formation areas (Fig. 5E). To further elucidate their osteogenic and angiogenic characteristics in vivo, the immunofluorescent staining of OPN and CD31 was performed. Consistent with previous findings, these two representative markers highly expressed in the new bone induced by the OxSF/ACP/PRP (Fig. 5F). This emphasized that the hydrogel seedbed possessed an outstanding osteogenic and angiogenic potential in vivo.

Furthermore, TEM analysis was applied to the cranial tissue samples at 14 days post-surgery to elucidate the biomineralization capacities of different composite hydrogels at the early stage of bone repair [43].

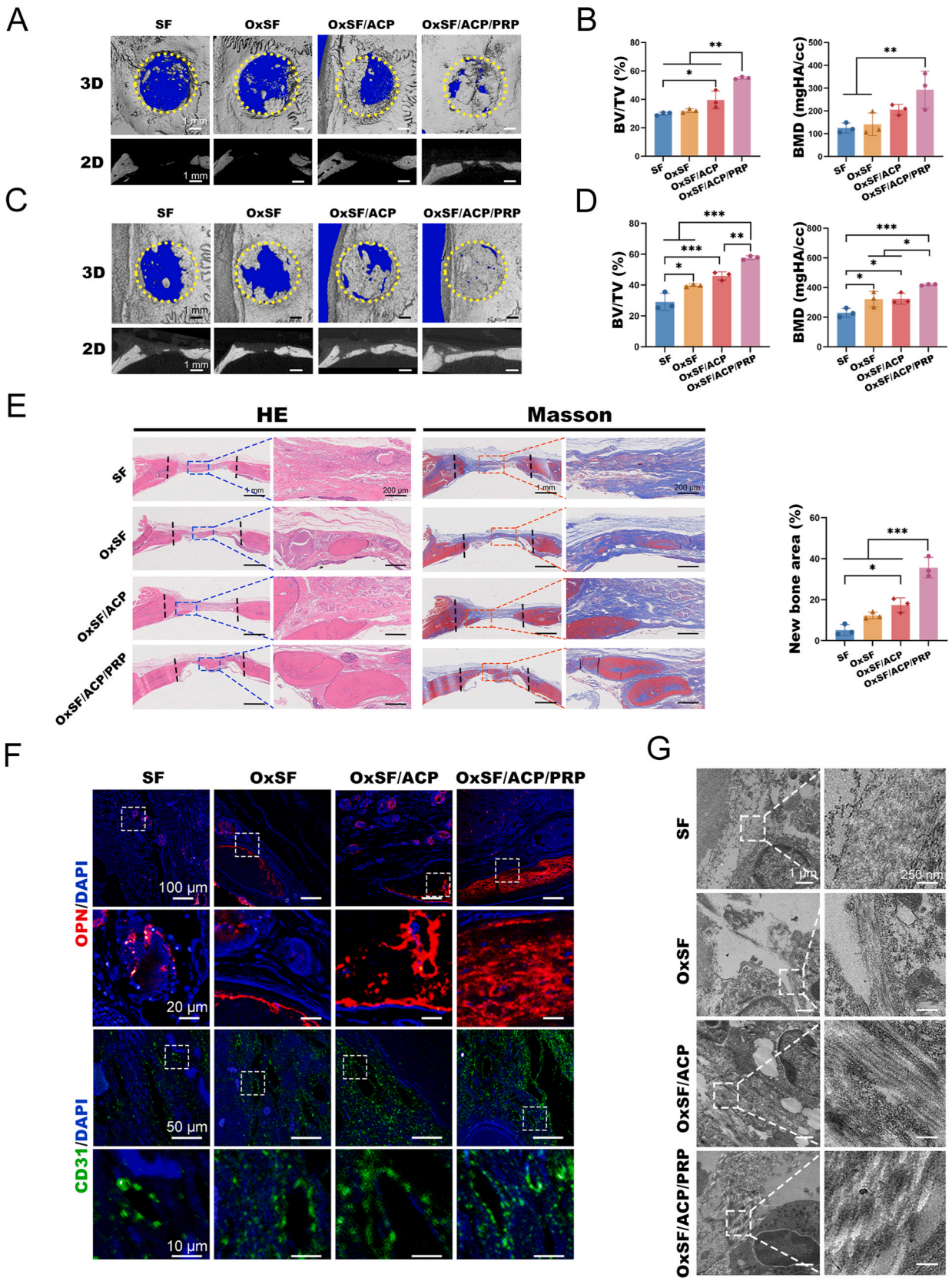

Fig. 5. The biomineralization hydrogel seedbed promoted vascularized bone regeneration in vivo. A) Radiological images and B) quantitative analysis of critical-sized cranial defects 8 weeks and C, D) 12 weeks post-surgery (Scale bar = 1 mm). E) Histological staining of cranial defect samples (Scale bar = 1 mm and 200 μm, respectively, dash lines representing the margin of the defect areas). F) Immunofluorescent staining of osteogenic (OPN) (Scale bar = 100 μm and 20 μm, respectively), and angiogenic (CD31) of the histological samples (Scale bar = 50 μm and 10 μm, respectively). G) TEM images representing the early-stage mineralization 14 days post-surgery (Scale bar = 1 μm and 250 nm, respectively). Error bars, mean ± standard deviation, *p < 0.05, **p < 0.01, ***p < 0.001.

TEM images revealed that the collagen matrix was deposited at the interface between the hydrogels and the adjacent repair tissues. Moreover, the seedbed hydrogel showed significantly highly-mineralized collagen at the interface while the other groups maintained relatively unmineralized extracellular matrix (Fig. 5G).

3.6. Exploration of underlying regulatory mechanism of osteogenesis related to the seedbed hydrogel

To elucidate the underlying mechanism of the superior osteogenesis of the seedbed hydrogel, an RNA transcriptome analysis was performed in BMSCs cultured with different hydrogel-conditioned medium. The RNAseq analysis revealed a notable heterogeneity in the BMSCs induced by different composite hydrogels, along with a pronounced concordance within the groups (Fig. S15). To explore the synergistic effect of ACP and PRP in the seedbed hydrogel, we conducted a Venn diagram for the upregulated differentially expressed genes (DEGs). Specifically, the blue circle represented DEGs upregulated by ACP, the green circle represented DEGs upregulated by PRP. These overlap genes were inside the red rectangle of the volcano plot that illustrated the integrated effect of ACP and PRP. These genes served as the most significant factor in the seedbed hydrogel (Fig. 6A). Intriguingly, two specific genes, namely SLC13A3 and MKX, were found to be upregulated in all the group comparisons (Fig. 6A). Considering our previous findings, these two genes emerged as putative correlates to the osteogenic potential induced by the composite hydrogel seedbed.

To confirm the insights gleaned from RNAseq analysis, we performed qPCR and Western blot analysis. The qPCR result of SLC13A3 concurred with the RNAseq result (Fig. 6B). While the mRNA expression of MKX exhibited an upregulation in the OxSF/ACP/PRP group compared to the OxSF and OxSF/ACP groups, discernible alterations failed to manifest in a statistically significant manner when contrasting the OxSF/ACP/PRP group with the SF group, as well as when comparing the OxSF and OxSF/ACP groups (Fig. 6B). The protein level also confirmed that the expression of SLC13A3 significantly increased while the expression of MKX remained merely unchanged (Fig. 6C). Thus, we mainly focused on the effect of SLC13A3 in the hydrogel seedbed instead of MKX.

SLC13A3 is a Na^+/dicarboxylate cotransporter located at the cell membrane [44]. Previous studies have found that this transporter is responsible for the binding and the transmembrane transport of succinate [45] (Fig. 6D), which plays a crucial role in metabolism, gene expression and cellular interaction [46]. Hence, we visualized the succinate uptake by introducing a customized FITC-conjugated succinate into the medium. As expected, the seedbed group prompted the greatest uptake of succinate into the cytoplasm of BMSCs (Fig. 6E). The SLC13A3 inhibitor, N-(P-amylcinnamoyl)anthranilic acid (NAA) [41], was applied and effectively reduced the succinate import in BMSCs (Fig. 6E). As the role of succinate in regenerative medicine remains controversial [45,47,48], we performed an ALP staining to elucidate the correlation between the SLC13A3 and the osteogenic potential of our

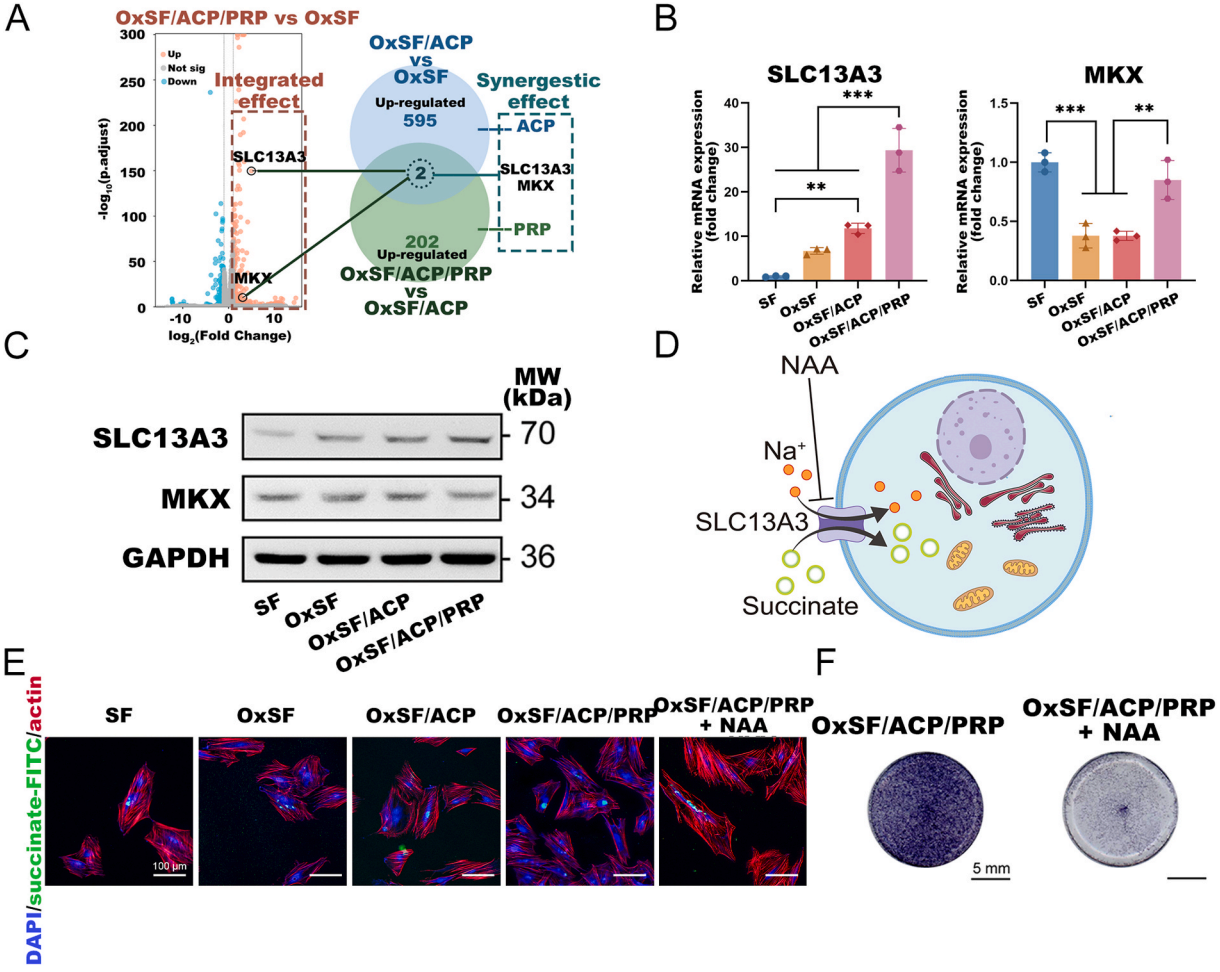

Fig. 6. The potential mechanism involved in the osteogenesis induced by the seedbed hydrogel. A) Venn diagram and volcano plot of the upregulated genes influenced by the seedbed hydrogel. B) Relative mRNA expression of SLC13A3 and MKX in BMSCs (n = 3). C) Expression of proteins SLC13A3 and MKX in BMSCs (normalization using GAPDH). D) Schematic diagram of the function of SLC13A3 and its inhibitor. E) Succinate uptake of BMSCs (Scale bar = 100 μm). F) ALP staining of BMSCs with or without inhibition of SLC13A3 (Scale bar = 5 mm). Error bars, mean ± standard deviation, $^{**}p < 0.01$, $^{***}p < 0.001$.

biomineralization seedbed. The ALP staining showed that the inhibition of SLC13A3 led to a reduced osteogenic potential in BMSCs (Fig. 6F). These results indicated that the intracellular transport of succinate through SLC13A3 plays a vital role in the osteogenesis induced by the designated seedbed hydrogel.

3.7. Exploration of the intracellular signaling pathway related to the seedbed hydrogel

To further investigate how the extracellular signals influence the intracellular signals, we performed multiple Kyoto Encyclopedia of Genes and Genomes (KEGG) enrichment (Fig. 7A) and Gene Ontology (GO) analysis (Fig. S16) on the DEGs, respectively. The enrichment analysis revealed that the PI3K-Akt signaling pathway is prominent as one of the few activated intracellular pathways (Fig. 7A), which is likely to contribute the most as the intracellular signaling pathway. Correspondingly, the gene set enrichment analysis (GSEA) confirmed that the PI3K-Akt signaling pathway plays an important role in the OxSF/ACP/PRP group (Fig. 7B). Western blotting result demonstrated an increase in the expression of phospho-Akt (*p*-Akt) in the OxSF/ACP/PRP group, which validates the involvement of PI3K-Akt signaling pathway in the osteogenic induction process of the seedbed system (Fig. 7C). The addition of MK2206, a validated inhibitor of *p*-Akt, led to a reduction in the expression of ALP (Fig. 7D).

To elucidate the relationship between the succinate transport and the PI3K-Akt signaling pathway, we subsequently examined the expression of *p*-Akt and Akt in the presence/absence of succinate. The exogenous succinate significantly upregulated the expression of *p*-Akt, especially at

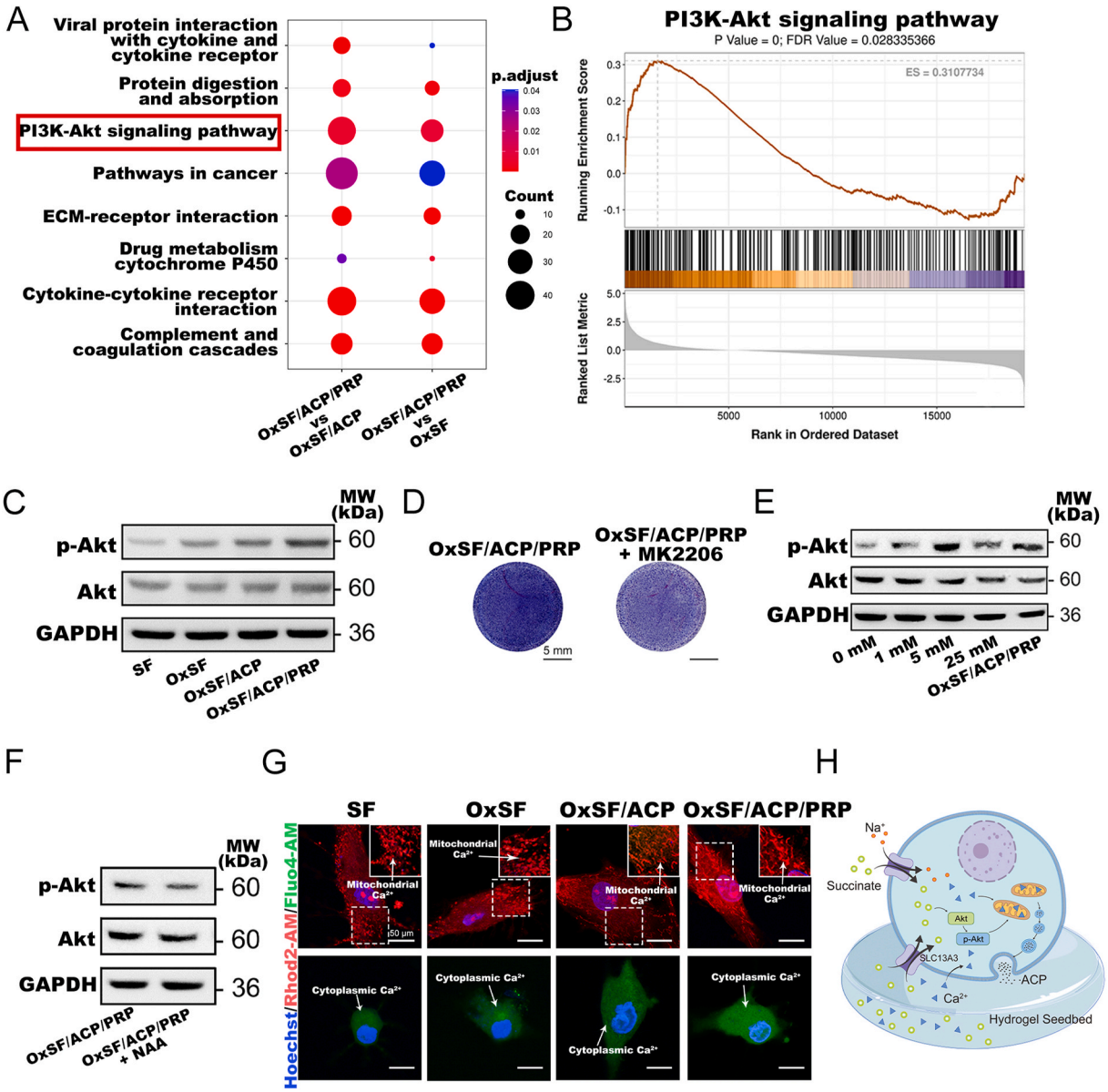

Fig. 7. The intracellular signaling pathway involved in the osteogenesis induced by the seedbed hydrogel. A) KEGG analysis of upregulated genes induced by the biomineralization seedbed. B) GSEA analysis of PI3K-Akt signaling pathway related features in the biomineralization seedbed. C) Western blotting of the activation of Akt and *p*-Akt in BMSCs (normalization using GAPDH). D) ALP staining of BMSCs with or without inhibition of PI3K-Akt signaling pathway (Scale bar = 5 mm). E) Western blotting of the activation of Akt and *p*-Akt in BMSCs with a gradient concentration of exogenous succinate or with the biomineralization seedbed. F) Western blotting of the activation of Akt and *p*-Akt with or without the inhibition of SLC13A3. G) The calcium distribution in mitochondria and cytoplasm in BMSCs (Scale bar = 100 μm). H) Schematic diagram of the regulation of the biomineralization hydrogel seedbed. Error bars, mean ± standard deviation, *p < 0.05, **p < 0.01, ***p < 0.001.

the concentration of 5 mM (Fig. 7E). This finding aligned with the optimal concentration of succinate reported in the literature for promoting osteogenic differentiation [49], which might be related to HIF-1α stabilization and subsequent PI3K-Akt signaling activation [50]. We further examined the succinate concentration in the supernatant of different composite hydrogels. The HPLC analysis verified the presence of exogenous succinate in the seedbed hydrogel, yet the concentration was significantly lower than the optimal concentration required for osteogenesis (Fig. 7E and S17). Building upon the upregulation of SLC13A3 (Fig. 6B and C), we speculated that the seedbed hydrogel simulated the osteogenic effects of exogenous succinate with intracellular transfer through its inherent properties, to some extent. The succinate-like function of the seedbed hydrogel could be a multifaceted outcome [51–53], with a significant role of PRP as well as the synergistic contribution of other components. On the one hand, the addition of the SLC13A3 inhibitor NAA impaired the phosphorylation of Akt (Fig. 7F), suggesting that the transport of succinate influences the osteogenic effect via the PI3K/Akt pathway. On the other hand, the expression of SLC13A3 was not significantly altered when the *p*-Akt inhibitor MK2206 was added into the culture medium (Fig. S18). The succinate also remained unaffected with the addition of MK2206 (Fig. S19). These results indicated that the increased succinate uptake by SLC13A3 led to the activation of PI3K/Akt signaling pathway.

Given that succinate is a vital metabolite in the mitochondrial electron transport chain [46], and mitochondrial plays a pivotal role in the ACP accumulation [54] and subsequent biomineralization [55–57], we further investigated the Ca^{2+} distribution in BMSCs. An influx of Ca^{2+} was observed from the cytoplasm to the mitochondria activated by the seedbed system (Fig. 7G). This phenomenon was reversed by adding NAA and MK2206 (Fig. S20), which indicated the potential influence of the succinate influx and PI3K/Akt signaling in the Ca^{2+} redistribution. Nevertheless, the Ca^{2+} in the cytoplasm remained stable (Fig. 7G and S20), which might be sourced from the exogenous ACP added in the seedbed. This process signified the conversion of exogenous ACP in the seedbed to the endogenous ACP within cells, providing continuous nutrients for biomineralization in critical-sized bone defect regeneration.

Overall, we proposed that the seedbed hydrogel promotes osteogenesis via an influx of succinate transported by SLC13A3, which further activates the PI3K/Akt signaling pathway. The activation of PI3K/Akt subsequently induced a Ca^{2+} redistribution into the mitochondria for endogenous ACP formation, leading to successful biomineralization (Fig. 7H).

4. Conclusion

In summary, we have established an engineered biomineralization seedbed system that combines robust geogrids and compact loam, enriched with organic and inorganic fertilizers. The designated double-network seedbed hydrogel displayed excellent mechanical properties and mimicked a biomineralization environment for constructing a stable scaffold in vitro. Moreover, the seedbed hydrogel exhibited a succinate-like function with the upregulation of SLC13A3, subsequently activating the PI3K/Akt signaling pathway. The intracellular signaling was speculated to increase the mitochondrial calcium uptake, leading to the conversion of the exogenous ACP into endogenous ACP and further promoting osteogenesis. The specialized seedbed hydrogel has demonstrated its effectiveness in promoting vascularized bone regeneration in vivo, offering a novel therapeutic approach for critical-sized bone defect regeneration.

5. Ethics approval and consent to participate

All the animal experiment procedures were approved by the Animal Care and Experiment Committee of the Ninth People's Hospital and animals were treated under standard specific pathogen-free laboratory conditions. The animal license number is SH9H-2019-A169-1.

CRediT authorship contribution statement

Yuhui Zhu: Writing – original draft, Visualization, Validation, Methodology, Investigation, Formal analysis, Data curation, Conceptualization. **Hao Gu:** Writing – original draft, Visualization, Validation, Methodology, Investigation, Formal analysis, Data curation, Conceptualization. **Jiawei Yang:** Writing – review & editing, Validation, Methodology, Investigation. **Anshuo Li:** Writing – review & editing, Validation, Methodology, Investigation. **Lingli Hou:** Methodology, Investigation. **Mingliang Zhou:** Writing – review & editing, Supervision, Methodology, Funding acquisition, Data curation, Conceptualization. **Xinquan Jiang:** Writing – review & editing, Supervision, Project administration, Funding acquisition, Conceptualization.

Declaration of Competing interest

The authors declare no conflict of interest.

Acknowledgements

This work is supported by the National Natural Science Foundation of China (No. 82130027, 81921002, 81991505, 31900971) and Cross Disciplinary Research Fund of Shanghai Ninth People's Hospital, Shanghai Jiao Tong University School of Medicine (JYJC202128). Moreover, we thank the Electron Microscopy center of Shanghai Institute of Precision Medicine, Shanghai Ninth People's Hospital, Shanghai Jiao Tong University School of Medicine, for their technical support and assistance in the electron microscopy.

Appendix A. Supplementary data

Supplementary data to this article can be found online at https://doi.org/10.1016/j.bioactmat.2024.01.024.

References

[1] G.L. Koons, M. Diba, A.G. Mikos, Materials design for bone-tissue engineering, Nat. Rev. Mater. 5 (2020) 584–603, https://doi.org/10.1038/s41578-020-0204-2.
[2] A. Woloszyk, Z.K. Tuong, L. Perez, L. Aguilar, A.I. Bankole, C.H. Evans, V. Glatt, Fracture hematoma micro-architecture influences transcriptional profile and plays a crucial role in determining bone healing outcomes, Biomater. Adv. 139 (2022) 213027, https://doi.org/10.1016/j.bioadv.2022.213027.
[3] W. Wang, K.W.K. Yeung, Bone grafts and biomaterials substitutes for bone defect repair: a review, Bioact. Mater. 2 (2017) 224–247, https://doi.org/10.1016/j.bioactmat.2017.05.007.
[4] N. Reznikov, J.A.M. Steele, P. Fratzl, M.M. Stevens, A materials science vision of extracellular matrix mineralization, Nat. Rev. Mater. 1 (2016), https://doi.org/10.1038/natrevmats.2016.41.
[5] C. Wang, K. Jiao, J. Yan, M. Wan, Q. Wan, L. Breschi, J. Chen, F.R. Tay, L. Niu, Biological and synthetic template-directed syntheses of mineralized hybrid and inorganic materials, Prog. Mater. Sci. 116 (2021) 100712, https://doi.org/10.1016/j.pmatsci.2020.100712.
[6] J. Li, J.F. Yan, Q.Q. Wan, M.J. Shen, Y.X. Ma, J.T. Gu, P. Gao, X.Y. Tang, F. Yu, J. H. Chen, F.R. Tay, K. Jiao, L.N. Niu, Matrix stiffening by self-mineralizable guided bone regeneration, Acta Biomater. 125 (2021) 112–125, https://doi.org/10.1016/j.actbio.2021.02.012.
[7] S. Yao, X. Lin, Y. Xu, Y. Chen, P. Qiu, C. Shao, B. Jin, Z. Mu, N.A.J.M. Sommerdijk, R. Tang, Osteoporotic bone Recovery by a highly bone-Inductive calcium phosphate Polymer-induced liquid-precursor, Adv. Sci. 6 (2019), https://doi.org/10.1002/advs.201900683.
[8] M. Maher, M. Castilho, Z. Yue, V. Glattauer, T.C. Hughes, J.A.M. Ramshaw, G. G. Wallace, Shaping collagen for engineering hard tissues: towards a printomics approach, Acta Biomater. 131 (2021) 41–61, https://doi.org/10.1016/j.actbio.2021.06.035.
[9] L.F. Echeverri, M.A. Herrero, J.M. Lopez, G. Oleaga, Early stages of bone Fracture healing: formation of a fibrin–collagen scaffold in the Fracture hematoma, Bull. Math. Biol. 77 (2015) 156–183, https://doi.org/10.1007/s11538-014-0055-3.
[10] X. Chen, H. Fan, X. Deng, L. Wu, T. Yi, L. Gu, C. Zhou, Y. Fan, X. Zhang, Scaffold structural microenvironmental cues to guide tissue regeneration in bone tissue

applications, Nanomaterials 8 (2018) 1–15, https://doi.org/10.3390/nano8110960.
[11] H. Schell, G.N. Duda, A. Peters, S. Tsitsilonis, K.A. Johnson, K. Schmidt-Bleek, The haematoma and its role in bone healing, J Exp Orthop 4 (2017), https://doi.org/10.1186/s40634-017-0079-3.
[12] D.N. Rockwood, R.C. Preda, T. Yücel, X. Wang, M.L. Lovett, D.L. Kaplan, Materials fabrication from Bombyx mori silk fibroin, Nat. Protoc. 6 (2011) 1612–1631, https://doi.org/10.1038/nprot.2011.379.
[13] K. Cao, Y. Zhu, Z. Zheng, W. Cheng, Y. Zi, S. Zeng, D. Zhao, H. Yu, Bio-Inspired Multiscale design for Strong and Tough biological Ionogels, Adv. Sci. 10 (2023) 1–10, https://doi.org/10.1002/advs.202207233.
[14] K. Zheng, J. Yu, W. Zhang, X. Li, Y. Fan, D.L. Kaplan, Self-assembling oxidized silk fibroin nanofibrils with controllable fractal dimensions, J. Mater. Chem. B 6 (2018) 4656–4664, https://doi.org/10.1039/c8tb00567b.
[15] R. Wu, H. Li, Y. Yang, Q. Zheng, S. Li, Y. Chen, Bioactive silk fibroin-based hybrid biomaterials for Musculoskeletal engineering: recent Progress and Perspectives, ACS Appl. Bio Mater. 4 (2021) 6630–6646, https://doi.org/10.1021/acsabm.1c00654.
[16] A. Noori, S.J. Ashrafi, R. Vaez-Ghaemi, A. Hatamian-Zaremi, T.J. Webster, A review of fibrin and fibrin composites for bone tissue engineering, Int J Nanomedicine 12 (2017) 4937–4961, https://doi.org/10.2147/IJN.S124671.
[17] G. Li, Y. Li, G. Chen, J. He, Y. Han, X. Wang, D.L. Kaplan, Silk-based biomaterials in Biomedical Textiles and fiber-based Implants, Adv Healthc Mater 4 (2015) 1134–1151, https://doi.org/10.1002/adhm.201500002.
[18] G. Griffanti, M.D. McKee, S.N. Nazhat, Mineralization of bone extracellular matrix-like scaffolds fabricated as silk Sericin-Functionalized dense collagen–fibrin hybrid hydrogels, Pharmaceutics 15 (2023), https://doi.org/10.3390/pharmaceutics15041087.
[19] B.W.M. de Wildt, R. van der Meijden, P.A.A. Bartels, N.A.J.M. Sommerdijk, A. Akiva, K. Ito, S. Hofmann, Bioinspired silk fibroin mineralization for Advanced in vitro bone Remodeling models, Adv. Funct. Mater. (2022), https://doi.org/10.1002/adfm.202206992.
[20] K. Zheng, Y. Chen, W. Huang, Y. Lin, D.L. Kaplan, Y. Fan, Chemically Functionalized silk for Human bone marrow-derived Mesenchymal stem cells proliferation and differentiation, ACS Appl. Mater. Interfaces 8 (2016) 14406–14413, https://doi.org/10.1021/acsami.6b03518.
[21] Z. Zhou, L. Zhang, J. Li, Y. Shi, Z. Wu, H. Zheng, Z. Wang, W. Zhao, H. Pan, Q. Wang, X. Jin, X. Zhang, R. Tang, B. Fu, Polyelectrolyte-calcium complexes as a pre-precursor induce biomimetic mineralization of collagen, Nanoscale 13 (2021) 953–967, https://doi.org/10.1039/d0nr05640e.
[22] Z. Mu, K. Chen, S. Yuan, Y. Li, Y. Huang, C. Wang, Y. Zhang, W. Liu, W. Luo, P. Liang, X. Li, J. Song, P. Ji, F. Cheng, H. Wang, T. Chen, Gelatin Nanoparticle-Injectable platelet-rich fibrin double network hydrogels with local Adaptability and bioactivity for enhanced osteogenesis, Adv Healthc Mater 9 (2020), https://doi.org/10.1002/adhm.201901469.
[23] W. Yin, X. Qi, Y. Zhang, J. Sheng, Z. Xu, S. Tao, X. Xie, X. Li, C. Zhang, Advantages of pure platelet-rich plasma compared with leukocyte- and platelet-rich plasma in promoting repair of bone defects, J. Transl. Med. 14 (2016) 1–19, https://doi.org/10.1186/s12967-016-0825-9.
[24] W. Cui, R. Zhu, A review on Tough Soft composites at different Length scales, Textiles 1 (2021) 513–533, https://doi.org/10.3390/textiles1030027.
[25] Y. Zhang, X. Pan, Z. Shi, H. Cai, Y. Gao, W. Zhang, Sustained release of stem cell factor in a double network hydrogel for ex vivo culture of cord blood-derived CD34 + cells, Cell Prolif. 51 (2018), https://doi.org/10.1111/cpr.12407.
[26] Y. Man, P. Wang, Y. Guo, L. Xiang, Y. Yang, Y. Qu, P. Gong, L. Deng, Angiogenic and osteogenic potential of platelet-rich plasma and adipose-derived stem cell laden alginate microspheres, Biomaterials 33 (2012) 8802–8811, https://doi.org/10.1016/j.biomaterials.2012.08.054.
[27] Y. Wei, M. Shi, J. Zhang, X. Zhang, K. Shen, R. Wang, R.J. Miron, Y. Xiao, Y. Zhang, Autologous Versatile Vesicles-incorporated biomimetic extracellular matrix induces biomineralization, Adv. Funct. Mater. 30 (2020), https://doi.org/10.1002/adfm.202000015.
[28] M. Li, M. Ogiso, N. Minoura, Enzymatic degradation behavior of porous silk fibroin sheets, Biomaterials 24 (2003) 357–365, https://doi.org/10.1016/S0142-9612(02)00326-5.
[29] A.C. Tas, S.B. Bhaduri, Rapid coating of Ti6Al4V at room temperature with a calcium phosphate solution similar to 10x simulated body fluid, J. Mater. Res. 19 (2004) 2742–2749, https://doi.org/10.1557/JMR.2004.0349.
[30] S. Lin, S. Yin, J. Shi, G. Yang, X. Wen, W. Zhang, M. Zhou, X. Jiang, Orchestration of energy metabolism and osteogenesis by Mg2+ facilitates low-dose BMP-2-driven regeneration, Bioact. Mater. 18 (2022) 116–127, https://doi.org/10.1016/j.bioactmat.2022.03.024.
[31] P. Zhou, X. Xie, D.P. Knight, X.H. Zong, F. Deng, W.H. Yao, Effects of pH and calcium ions on the conformational transitions in silk fibroin using 2D Raman correlation spectroscopy and 13C solid-state NMR, Biochemistry 43 (2004) 11302–11311, https://doi.org/10.1021/bi049344i.
[32] Z. Yang, Z. Yang, L. Ding, P. Zhang, C. Liu, D. Chen, F. Zhao, G. Wang, X. Chen, Self-adhesive hydrogel biomimetic Periosteum to promote critical-size bone defect repair via synergistic osteogenesis and angiogenesis, ACS Appl. Mater. Interfaces 14 (2022) 36395–36410, https://doi.org/10.1021/acsami.2c08400.
[33] G. Irmak, M. Gümüşderelioğlu, Patients- and tissue-specific bio-inks with photoactivated PRP and methacrylated gelatin for the fabrication of osteochondral constructs, Mater. Sci. Eng. C 125 (2021), https://doi.org/10.1016/j.msec.2021.112092.
[34] D.M. Dohan Ehrenfest, L. Rasmusson, T. Albrektsson, Classification of platelet concentrates: from pure platelet-rich plasma (P-PRP) to leucocyte- and platelet-rich fibrin (L-PRF), Trends Biotechnol. 27 (2009) 158–167, https://doi.org/10.1016/j.tibtech.2008.11.009.
[35] Z. Geng, L. Ji, Z. Li, J. Wang, H. He, Z. Cui, X. Yang, C. Liu, Nano-needle strontium-substituted apatite coating enhances osteoporotic osseointegration through promoting osteogenesis and inhibiting osteoclastogenesis, Bioact. Mater. 6 (2021) 905–915, https://doi.org/10.1016/j.bioactmat.2020.09.024.
[36] T. Kokubo, H. Takadama, How useful is SBF in predicting in vivo bone bioactivity? Biomaterials 27 (2006) 2907–2915, https://doi.org/10.1016/j.biomaterials.2006.01.017.
[37] A.R. Wufsus, K. Rana, A. Brown, J.R. Dorgan, M.W. Liberatore, K.B. Neeves, Elastic behavior and platelet retraction in low- and high-density fibrin gels, Biophys. J. 108 (2015) 173–183, https://doi.org/10.1016/j.bpj.2014.11.007.
[38] S.L. Rowe, J.P. Stegemann, Microstructure and Mechanics of collagen-fibrin matrices polymerized using Ancrod Snake Venom enzyme, J. Biomech. Eng. 131 (2009) 133–154, https://doi.org/10.1115/1.3128673.
[39] J. Wang, G. Yang, Y. Wang, Y. Du, H. Liu, Y. Zhu, C. Mao, S. Zhang, Chimeric protein template-induced shape control of bone mineral nanoparticles and its Impact on Mesenchymal stem cell fate, Biomacromolecules 16 (2015) 1987–1996, https://doi.org/10.1021/acs.biomac.5b00419.
[40] D. Wang, Y.X. Feng, M. Li, S. Guo, Y. Jiang, Seeded mineralization in silk fibroin hydrogel matrices leads to continuous rhombohedral CaCO3 films, Crystals 10 (2020), https://doi.org/10.3390/cryst10030166.
[41] Y. Brudno, A.B. Ennett-Shepard, R.R. Chen, M. Aizenberg, D.J. Mooney, Enhancing microvascular formation and vessel maturation through temporal control over multiple pro-angiogenic and pro-maturation factors, Biomaterials 34 (2013) 9201–9209, https://doi.org/10.1016/j.biomaterials.2013.08.007.
[42] Y. Xu, G. Shi, J. Tang, R. Cheng, X. Shen, Y. Gu, L. Wu, K. Xi, Y. Zhao, W. Cui, L. Chen, ECM-inspired micro/nanofibers for modulating cell function and tissue generation, Sci. Adv. 6 (2020) 1–18, https://doi.org/10.1126/sciadv.abc2036.
[43] F. Passaretti, M. Tia, V. D'Esposito, M. De Pascale, M. Del Corso, R. Sepulveres, D. Liguoro, R. Valentino, F. Beguinot, P. Formisano, G. Sammartino, Growth-promoting action and growth factor release by different platelet derivatives, Platelets 25 (2014) 252–256, https://doi.org/10.3109/09537104.2013.809060.
[44] S. Yin, W. Zhang, Z. Zhang, X. Jiang, Recent Advances in scaffold design and material for vascularized tissue-engineered bone regeneration, Adv Healthc Mater 8 (2019) 1–19, https://doi.org/10.1002/adhm.201801433.
[45] H. Liao, H.P. Yu, W. Song, G. Zhang, B. Lu, Y.J. Zhu, W. Yu, Y. He, Amorphous calcium phosphate nanoparticles using adenosine triphosphate as an organic phosphorus source for promoting tendon–bone healing, J Nanobiotechnology 19 (2021) 1–17, https://doi.org/10.1186/s12951-021-01007-y.
[46] K. Liang, C. Zhao, C. Song, L. Zhao, P. Qiu, S. Wang, J. Zhu, Z. Gong, Z. Liu, R. Tang, X. Fang, Y. Zhao, In situ biomimetic mineralization of bone-like hydroxyapatite in hydrogel for the acceleration of bone regeneration, ACS Appl. Mater. Interfaces (2022) 1–15, https://doi.org/10.1021/acsami.2c16217.
[47] B. Hersant, M. Sid-Ahmed, L. Braud, M. Jourdan, Y. Baba-Amer, J.P. Meningaud, A. M. Rodriguez, Platelet-rich plasma improves the wound healing potential of Mesenchymal stem cells through Paracrine and metabolism alterations, Stem Cells Int 2019 (2019), https://doi.org/10.1155/2019/1234263.
[48] M. Shen, C. Wang, D. Hao, J. Hao, Y. Zhu, X. Han, L. Tonggu, J. Chen, K. Jiao, F. R. Tay, L. Niu, Multifunctional Nanomachinery for Enhancement of bone healing, Adv. Mater. 34 (2022) 1–12, https://doi.org/10.1002/adma.202107924.
[49] H. Mao, A. Yang, Y. Zhao, L. Lei, H. Li, Succinate supplement Elicited "pseudohypoxia" condition to promote proliferation, migration, and osteogenesis of Periodontal Ligament cells, Stem Cells Int 2020 (2020), https://doi.org/10.1155/2020/2016809.
[50] Z. Zhang, L. Yao, J. Yang, Z. Wang, G. Du, PI3K/Akt and HIF-1 signaling pathway in hypoxia-ischemia, Mol. Med. Rep. 18 (2018) 3547–3554, https://doi.org/10.3892/mmr.2018.9375.
[51] F. Grimolizzi, L. Arranz, Multiple faces of succinate beyond metabolism in blood, Haematologica 103 (2018) 1586–1592, https://doi.org/10.3324/haematol.2018.196097.
[52] L. Bunse, S. Pusch, T. Bunse, F. Sahm, K. Sanghvi, M. Friedrich, D. Alansary, J. K. Sonner, E. Green, K. Deumelandt, M. Kilian, C. Neftel, S. Uhlig, T. Kessler, A. von Landenberg, A.S. Berghoff, K. Marsh, M. Steadman, D. Zhu, B. Nicolay, B. Wiestler, M.O. Breckwoldt, R. Al-Ali, S. Karcher-Bausch, M. Bozza, I. Oezen, M. Kramer, J. Meyer, A. Habel, J. Eisel, G. Poschet, M. Weller, M. Preusser, M. Nadji-Ohl, N. Thon, M.C. Burger, P.N. Harter, M. Ratliff, R. Harbottle, A. Benner, D. Schrimpf, J. Okun, C. Herold-Mende, S. Turcan, S. Kaulfuss, H. Hess-Stumpp, K. Bieback, D. P. Cahill, K.H. Plate, D. Hänggi, M. Dorsch, M.L. Suvà, B.A. Niemeyer, A. von Deimling, W. Wick, M. Platten, Suppression of antitumor T cell immunity by the oncometabolite (R)-2-hydroxyglutarate, Nat Med 24 (2018) 1192–1203, https://doi.org/10.1038/s41591-018-0095-6.
[53] Y. Guo, C. Xie, X. Li, J. Yang, T. Yu, R. Zhang, T. Zhang, D. Saxena, M. Snyder, Y. Wu, X. Li, Succinate and its G-protein-coupled receptor stimulates osteoclastogenesis, Nat. Commun. 8 (2017) 1–12, https://doi.org/10.1038/ncomms15621.
[54] D. Pei, J. Sun, C. Zhu, F. Tian, K. Jiao, M.R. Anderson, C. Yiu, C. Huang, C. Jin, B. E. Bergeron, J. Chen, F.R. Tay, L. Niu, Contribution of Mitophagy to cell-Mediated mineralization: Revisiting a 50-Year-old Conundrum, Adv. Sci. 5 (2018), https://doi.org/10.1002/advs.201800873.

[55] M.J. Akhtar, S.A. Khan, B. Kumar, P. Chawla, R. Bhatia, K. Singh, Role of sodium dependent SLC13 transporter inhibitors in various metabolic disorders, Mol. Cell. Biochem. 478 (2023) 1669–1687, https://doi.org/10.1007/s11010-022-04618-7.
[56] L. Peruzzotti-Jametti, J.D. Bernstock, N. Vicario, A.S.H. Costa, C.K. Kwok, T. Leonardi, L.M. Booty, I. Bicci, B. Balzarotti, G. Volpe, G. Mallucci, G. Manferrari, M. Donegà, N. Iraci, A. Braga, J.M. Hallenbeck, M.P. Murphy, F. Edenhofer, C. Frezza, S. Pluchino, Macrophage-derived extracellular succinate licenses Neural stem cells to Suppress Chronic Neuroinflammation, Cell Stem Cell 22 (2018) 355–368, https://doi.org/10.1016/j.stem.2018.01.020.
[57] T. Iwayama, T. Okada, T. Ueda, K. Tomita, S. Matsumoto, M. Takedachi, S. Wakisaka, T. Noda, T. Ogura, T. Okano, P. Fratzl, T. Ogura, S. Murakami, Osteoblastic lysosome plays a central role in mineralization, Sci. Adv. 5 (2019) 1–10, https://doi.org/10.1126/sciadv.aax0672.